OPEN ACCESS
IOP Publishing
Journal of Physics D: Applied Physics
J. Phys. D: Appl. Phys. **55** (2022) 295301 (19pp)
https://doi.org/10.1088/1361-6463/ac677a

Confronting Vegard's rule in $Ge_{1-x}Sn_x$ epilayers: from fundamentals to the effect of defects

S Magalhães[1,*], M Dias[1], B Nunes[1], F Oliveira[2], M F Cerqueira[2,3] and E Alves[1]

[1] IPFN, Instituto de Plasmas e Fusão Nuclear, Campus Tecnológico e Nuclear, Instituto Superior Técnico, Universidade de Lisboa, Estrada Nacional 10, 2695-066 Bobadela LRS, Portugal
[2] Centro de Física, Universidade do Minho, Campus de Gualtar, 4710-057 Braga, Portugal
[3] International Iberian Nanotechnology Laboratory, Braga, Portugal

E-mail: smagalhaes@ctn.tecnico.ulisboa.pt

Received 15 December 2021, revised 10 April 2022
Accepted for publication 14 April 2022
Published 3 May 2022

Abstract

Comprehensive and systematic study challenging the application of Vegard's rule to germanium tin solid solutions grown on germanium buffer layers and 100 silicon substrates is presented. The binary's lattice parameters, composition and respective uncertainties are determined through x-ray diffraction via reciprocal space mapping technique employing newly developed software. The tin content is confirmed by Rutherford backscattering spectrometry and energy dispersive x-ray spectroscopy. The statistical agreement between the tin contents derived by the different structural characterization techniques suggests the binary to follow generically the Vegard's rule in the range of low Sn molar fractions (<5%). Phase separation, Sn segregation, point defects, post-growing oxygen impurities, and deteriorated surface morphology are found to be relevant within the ∼200 nm germanium tin films. Although, complex mechanisms triggering composition/strain heterogeneities are found in the analysed $Ge_{1-x}Sn_x$ compounds, the deviation from the perfect crystals is suggested to be not enough to distort the in- and out-of-plane lattice parameters away from its empirical linear combination.

Supplementary material for this article is available online

Keywords: GeSn compound, x-ray diffraction, x-ray reflectivity, defects, ion channelling

(Some figures may appear in colour only in the online journal)

1. Introduction

Germanium tin (GeSn) and silicon germanium tin (SiGeSn) are examples of solid solutions based group-IV crystalline semiconductors. The binary and the ternary have been the objects of intense research in the last two decades mainly due to the possibility of making a silicon-compatible direct band gap material with controlled lattice parameters and band gap energy [1–10]. The possibility of epitaxial growth directly on silicon substrates further motivates the research in the field despite the significantly different thermodynamic properties, ionic sizes and electronegativities of Si, Ge and Sn. In fact, the nature of the different atoms challenges the growth of single phase $Ge_{1-x}Sn_x$ with excellent crystalline quality. The crystalline quality deteriorates with increasing tin content as phase separation and segregation tend to decrease the solubility for higher Sn content SiGeSn pure random compounds (<0.5%) [11]. Even for low Sn content GeSn (or SiGeSn), the relaxation of lattice strain in the epitaxial buffer layers acting as virtual substrates decreases the pseudomorphism degree while are often accompanied by layer tilting and development and

* Author to whom any correspondence should be addressed.

propagation of dislocations [12]. The lack of solubility in the compound, on the one hand, affects the crystal size through a heterogeneous distribution of unit cells with slightly different lattice parameters. On the other hand, it limits the crystalline quality because of strain relaxation via defects' formation. Composition and/or strain heterogeneities strongly affect the growing of quasi-perfect single crystalline GeSn (or SiGeSn) compound layered structures. Both crystalline quality limitations have similar effects in the x-ray diffraction (XRD) patterns. Specifically, in the case of ω- or 2θ–ω (radial) scans, composition and strain shift the Bragg peaks. In fact, both set-ups are influenced by the lattice strain propagation due to deviations from the ideal pseudomorphic growth and because of defects in the semiconductor epitaxial layers. With respect to crystallographic defects, highly mosaic crystals foresee the broadening of the Bragg peaks. Therefore, it decreases the accuracy in the determination of the centroid peak. Executing reciprocal space mapping (RSM) of asymmetric reflections may overcome the above ambiguity by enabling the separation of the composition and strain related effects so that the Bragg peak positions can be precisely derived in the reciprocal space [13–18]. The determination with high accuracy of the lattice parameters and the $(Si_{1-y}Ge_y)_{1-x}Sn_x$ stoichiometry (x and y) is, thus, fundamental to understand the relaxation mechanism(s) responsible for the crystalline quality deterioration with increasing Sn content. Corrections to the Vegard's rule are known for the $Ge_{1-x}Sn_x$ and the $Si_{1-x}Ge_x$ cubic systems as well as for $(Si_{1-y}Ge_y)_{1-x}Sn_x$ where bowing parameters are incorporated into the linear relationship between the individual lattice parameters (band-gaps) [19, 20]. Furthermore, calculations based on the density functional theory support the deviation observed in both $Ge_{1-x}Sn_x$ and $Si_{1-y}Ge_y$ systems [21, 22]. To the best knowledge of the authors, it is the first time a systematic experimental analysis devoted to the validation of Vegard's rule in the $Ge_{1-x}Sn_x$ compounds is put forward considering all relevant uncertainties. Impurities also distort the crystal lattice imposing a non-linearity of the relation between the lattice parameters and the derived composition [23–25]. In order to evaluate the composition, new software (method) to fit mathematically the RSMs employing 2D Gaussians is presented and made available to the scientific community. Besides the 2D fitting, the software provides the option of fitting the projections onto both orthogonal directions using Gaussians and pseudo-Voigt (PV) functions. From the RSM software, the lattice parameters of the Si substrate, Ge buffer layer and GeSn compound as well as its uncertainties are determined. The composition of the binary layer is then derived together with its uncertainty. Results obtained with prior versions of the software can be found elsewhere [14–17, 26, 27]. The software titled RSM can be found at www.mrox.eu and is addressed in supplementary information (S1) (available online at stacks.iop.org/JPhysD/55/295301/mmedia) where full description is presented. The crystal growing procedure of a set of GeSn compound epilayers by molecular beam epitaxy (MBE) on a Si substrate and the experimental characterization techniques are described in section 2. Section 3 is devoted to the demonstration of the proposed analytical method. In section 4, the composition and strain dependency upon the Sn content is characterized by the x-ray RSM, x-ray 2θ–ω scans, x-ray reflectivity (XRR), ion and electron beam measurements. Reasonable discrepancies in the determination of the molar fraction of several systems using XRD and Rutherford backscattering spectrometry (RBS) (ex, the $Al_{1-x}In_xN$) have been reported [28, 29]. The studies refer to high density of defects build-up hydrostatic strain into the layers, thus, motivating analogous analysis in the current manuscript. The main conclusions of the manuscript are addressed in section 5.

2. Samples and description of the experimental techniques

A set of four samples (C1, C2, C3 and C4) were grown by MBE using an electron beam evaporator for germanium with a silicon crucible and a Knudsen cell for the tin with pyrolytic BN crucible and a base pressure lower than 10^{-9} mbar [30, 31]. Substrates of 100 silicon with 100 mm diameter were used. They were treated with a wet-chemical etching in a HF bath, to clean and create a hydrogenized layer at the surface, and when inside the deposition chamber, the substrate was heated to 700 °C to remove the hydrogenized layer by thermal desorption. This treatment was followed by the growth at 330 °C of an epitaxial buffer layer of Ge with a thickness of ∼100 nm and a growth rate of 0.43 Å s^{-1}. The substrate temperature was reduced to 75 °C and 85 °C to grow a $Ge_{1-x}Sn_x$ layer with a thickness of ∼200 nm over the buffer layer. This layer was grown with the same Ge flux as the one used for the buffer layer whereas the Sn flux was increased from sample to sample (from C1 up to C4). A low temperature was used to grown the $Ge_{1-x}Sn_x$ layer in order to mitigate tin aggregation and/or precipitation. The samples were finalized with a annealing step *in-situ* by ramping-up their temperature to ≈195 °C followed by an immediate ramp-down to room temperature (see figure 1).

The relaxed in-plane ($a_{||}$) and out-of-plane ($a_{\perp}$) lattice parameters of the single elements materials (Si and Ge and Sn cubic crystals) as well as relevant stiffness coefficients (C_{13} and C_{33}) are listed in table 1. The values depicted in table 1 reflect the average determined for the last two decades of the published parameters found in the literature. An exhaustive comparison between the in- and out-of-plane Si, Ge and Sn lattice parameters as well as respective stiffness coefficients is addressed in S2.

The samples were analysed by XRD/XRR, RBS/ion channelling (RBS/C), backscattered electron imaging (BSE) and secondary electron imaging (SE). Although the Sn contents derived from XRD, RBS and energy dispersive x-ray spectroscopy (EDS) were measured in the same region of the sample, the beam dimensions are different for each technique and lateral composition heterogeneities are not to be discarded. With respect to the XRD technique, RSM and MROX software's were used. Related to the former, it is first time the software is presented as final version to the scientific community. The latter, acronym for multiple reflection optimization package for XRD, in its single reflection mode has been often used

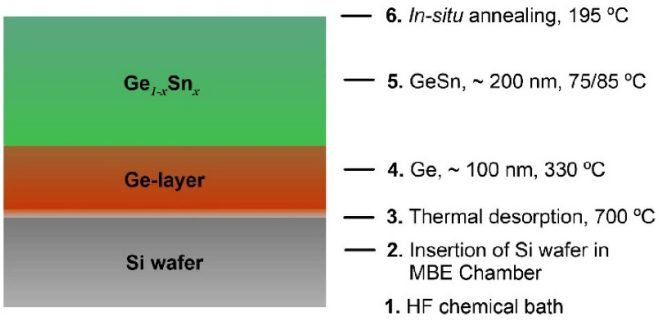

Figure 1. Illustration of the samples' growth steps. The numeration indicates the proceeding order.

for the simulation (and fitting) of the 2θ–ω scans using the dynamical theory of XRD [32–38] while the multiple reflection mode has been recently presented [38]. The code employs the dynamical theory of XRD and considers the effects of the instrumental function and the presence of Cu Kα_2. In particular, de-convoluting a layered structure with specific composition, thickness and crystalline quality determined via the static Debye–Waller (DW) factor into several layers allows deepening the knowledge on the ternary's solubility. With respect to XRR, a developed code to be fully integrated into the MROX main software was developed. Several publications fall into prior versions of the software can be found elsewhere [39, 40]. The XRD/XRR measurements were performed on a Bruker D8 AXS diffractometer. At the primary x-ray beam side, a Cu source was used together with a Göbel mirror and a germanium 220 monochromator in order to reduce the vertical divergence and to mitigate the Kα_2 radiation, respectively. A double-axis set-up was used, where a slit of 0.1 mm width faces the detector to perform the radial 2θ–ω scans and the reciprocal space maps. To probe the ω-scans, in particular to optimize the final measurements, no slit was placed before the detector. With respect to the XRR measurements, the 220 Ge monochromator was replaced by a Soller slit in order to maximize the reflected intensity. The diffracted/reflected intensity was collected with a point focus detector and recorded with the Bruker D8 AXS diffractometer acquisition software. RBS/C measurements were performed on a van de Graaff AN-2500 type-A accelerator using a 2 MeV $^4He^+$ ion beam of 1 mm diameter. A pin diode was placed at a backscattering angle of $-165°$ to collect the backscattered particles. Random RBS spectra were acquired by tilting the surface normal by 5° away from the analysing beam and rotating the sample during the measurement to suppress channelling effects. Simulations of the random RBS spectra were performed using the Nuno's data furnace (NDF) code [41]. The crystalline quality of the GeSn epilayers along the growing direction are determined from the axial <001> aligned scans by $^4He^+$ ion channelling measurements [42]. The XRD as well as the RBS/C measurements were performed at the Laboratório de Aceleradores e Tecnologias de Radiação, Campus Tecnológico e Nuclear, Lisbon, Portugal. The BSE and SE modes were performed using a JEOL JSM-7001F field emission gun scanning electron microscope equipped with an Oxford Instruments EDS system. Quantitative analysis was performed by EDS using appropriate trademarked software. Each sample was analysed in more than ten randomly selected points. The EDS measurements were executed in the Electron Microscopy Laboratory (Microlab) at the Instituto Superior Técnico, Lisbon, Portugal.

Table 1. Si, Ge and Sn in- ($a_{||}$) and out-of-plane ($a_\perp$) relaxed lattice parameters, and C_{13} and C_{33} stiffness coefficients used to determine the Sn contents in the $Ge_{1-x}Sn_x$ binary compounds.

Element	$a_{\|\|}$ (Å)	$a_\perp$ (Å)	C_{13} (GPa)	C_{33} (GPa)
Si	5.431	5.431	63.9	165.7
Ge	5.658	5.658	47.9	129.2
Sn	6.49	6.49	29.3	67.6

3. Determination of the lattice parameters, composition and respective uncertainties to sample C4—application of the RSM software

The fitting of the RSM around the 115 Si, 115 Ge and 115 $Ge_{1-x}Sn_x$ reciprocal lattice points were successfully accomplished through the developed RSM software. The software fits the experimental data employing a Marquardt–Levenberg algorithm [43]. Furthermore, it employs 2D-Gaussians taking into consideration the rotation of the diffraction spots in the reciprocal space. The software is applicable to asymmetric reflections as the case presented here but, furthermore, to symmetric reflections. The best solution found is refined using PV functions of the cuts along the measured domain. Cubic and hexagonal (wurtzite) Bravais lattices are implemented in the code. The software determines the $(Q_{\hat{x}}, Q_{\hat{z}})$ centroids of the diffraction spots [44]. Thus, the crystal lattice in- and out-of-plane lattice parameters and chemical composition as well as the relevant uncertainties are determined using the Bragg's rule and the Poisson law in order consider the biaxial strain [45–47]. Furthermore, the determination of $\delta Q_{\hat{x}}$ and $\delta Q_{\hat{z}}$, i.e, the widths of the diffraction spots along Q_x and Q_z, respectively, allows quantifying the crystalline mosaicity of a given crystal. The limitations of the RSM software are only restricted to an almost complete overlap diffraction spots where respective centres may not be accurately determined. The procedure to determine the lattice parameters of the tri-layer heteroepitaxial system exhaustively described in S3 is exemplified using the highest Sn content $(Si_{1-y}Ge_y)_{1-x}Sn_x$ layer grown on a $Si_{1-y}Ge_y$ buffer layer and a 100 silicon substrate (sample C4). The choice of sample C4 is based upon the fact that the 115 $Si_{1-y}Ge_y$ and 115 $(Si_{1-y}Ge_y)_{1-x}Sn_x$ ellipsoids (diffraction spots) are, as shown in figure 2, perfectly distinguishable. The experimental 115 RSM is depicted in figure 2(a)) while its simulation is plotted in figure 2(b)). The intensity scale on the right side of figure 2 is calculated as $\log(I_0 + 1)$, where I_0 is the measured intensity. The logarithmic representation for the intensity emphasizes the differences between the diffraction patterns of all involved crystals while the increment of the unity in the logarithmic argument overcomes the $\log(I_0 \to 0)$ mathematical impossibility.

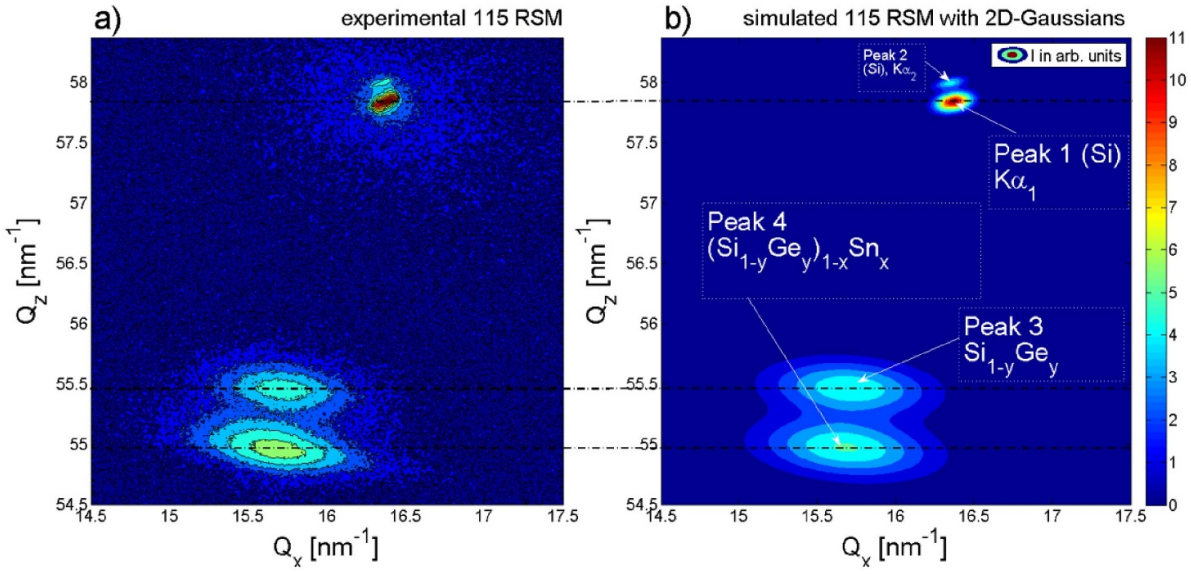

Figure 2. Experimental RSM in the vicinities of the 115 Si reciprocal lattice point and simulated RSM using 2D-Gaussians of the highest tin content $(Si_{1-y}Ge_y)_{1-x}Sn_x$ sample.

The indexation of the various diffraction spots is highlighted in figure 2(b). Peak #1 refers to the Cu Kα_1 115 Si diffraction spot while peak #2 is associated to the Cu Kα_2 115 Si. In fact, the Cu Kα_2 115 Si residuals were not completely mitigated by the optical system (Göbel mirror and 2-bounce 220 Ge monochromator). Placing an analyser at the secondary x-ray beam-path would further decrease the intensity associated to peak #2 but at the expenses of ∼1 magnitude order of intensity decrease to the Cu Kα_1 115 Si as well. Peaks #1 and #2 appear rotated while the 115 $Si_{1-y}Ge_y$ (peak #3) one presents very low level of rotation. Peak #4 is attributed to the 115 diffraction of the $(Si_{1-y}Ge_y)_{1-x}Sn_x$ pseudo-ternary. The horizontal dash-dot black lines crossing figures 2(a) and (b) mark the Q_z positions of the 115 Si substrate, $Si_{1-y}Ge_{y1-x}$ and $(Si_{1-y}Ge_y)_{1-x}Sn_x$, from higher to lower Q_z, respectively. The simulated Q_z positions using equation S3.1 agree perfectly with the experimental data. Moreover, the shape of all diffraction spots is well simulated with the 2D-Gaussians. The slight differences between the experimental data and the simulation are focussed on the intensity (colour distribution) and widths of the diffraction spots. With respect to the former, the most visible differences arise from the distribution of the intensities in the reciprocal space attributed to the 115 Si (peak #1) and centre of the 115 $(Si_{1-y}Ge_y)_{1-x}Sn_x$ diffraction spot (peak #4). Nevertheless, the distribution of the levels of intensity through colours may induce ambiguities as simulated data is less clear under the 2D representation rather than 1D cut along a specific direction. What is more, typical problems originated by the big data analysis play an important role. In fact, individual RSM contains more than 20 000 (Q_x, Q_z, I) pairs adding extra computational efforts to the fitting process. In order to check the validity of the 2D-Gaussian in the angular region of interest (vicinities of the Bragg peaks), the proposed method refines the fitting of the RSM with PV functions of the individual cuts. Moreover, the advantage of employing the latter in the current work is related to the determination of the uncertainties through a fast fitting method rather than the time-consuming 2D-Gaussian fitting. In fact, a cut along a specific direction presents more than 50 times less experimental data points reducing dramatically the time for the convergence of the fitting. Figure 3 compares the fittings performed with the Gaussian and PV functions along the red and green lines for the 115 Si Kα_1 (peak #1), (a), 115 Si Kα_2 (peak #2), (b), 115 $Si_{1-y}Ge_{y1-x}$ (peak #3), (c) and 115 $(Si_{1-y}Ge_y)_{1-x}Sn_x$ (peak #4), (d) diffraction spots, respectively. The better fit quality obtained using PVs compared to the Gaussians, especially around the various peaks tails is evidenced in figure 3. ω- as well as 2θ–ω scans constitute specific cuts along the asymmetric RSM [48]. In fact, according to [49], the mathematical peak-function which better describes both measurements is the PV, thus, by virtue of the reciprocity theorem, it applies to the RSM as well. To summarize, from the $Q_{\hat{x}}, Q_{\hat{z}}$ centres derived from the 2D-Gaussian and PV fittings, the in- and out-of-planes lattice parameters are determined (equations S3.2(a_1) and (a_2)). In the case of sample C4, $(Q_x, Q_z) = (15.6791, 54.9857)$, thus, $a_{\parallel} = 5.6673 \pm 0.0041$ Å and $a_{\perp} = 5.7135 \pm 0.0021$ Å. Assuming a Ge relaxed lattice parameter of 5.658 Å (table 1) the measured quantities reveal higher lattice parameters evidencing the effect of the growing of the pseudo-ternary and the limited Ge buffer layer crystal size (∼100 nm). Composition is then determined using equations S3.3–S3.5. To determine the composition a combination of a bisection, secant and inverse quadratic interpolation methods are employed [50, 51]. The procedure to derive the lattice parameters, composition and associated uncertainties using the RSM software is composed by IV steps exhaustively described in S3. In the case of sample C4, $x_{Sn} = 0.042 \pm 0.006$. Finally, the uncertainties in the Si, $Si_{1-x}Ge_x$ relaxed lattice parameters, respective stiffness coefficients and measured lattice parameters are

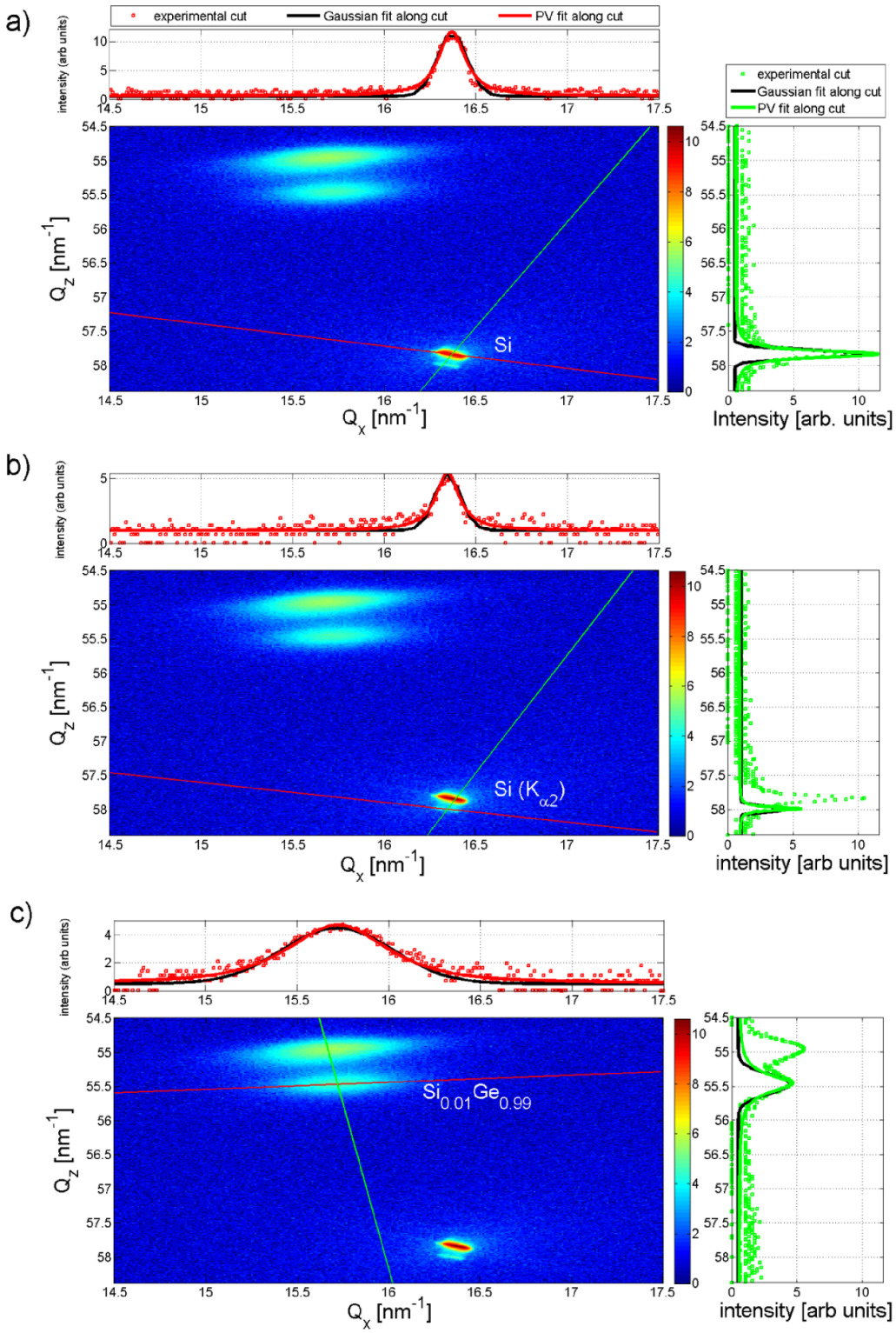

Figure 3. Representation of the cuts along specific directions determined using equation (1) of the experimental RSM highlighting the 115 Si Kα_1, (a), 115 Si Kα_2, (b), the $Si_{1-y}Ge_y$ binary, (c), and the $(Si_{1-y}Ge_y)_{1-x}Sn_x$ pseudo ternary, (d), respectively. Upper: cut of the RSM experimental data along the red line and fit using a Gaussian and PV functions. Right: cut of the RSM experimental data along the green line and fit using a Gaussian and PV functions. (e) Ge content in $Si_{1-y}Ge_y$ derived using the proposed method. (f) Sn content in $(Si_{1-y}Ge_y)_{1-x}Sn_x$ derived using the proposed method for sample C4.

considered to derive the uncertainties in the Sn content (0.006). The uncertainties in y_{Ge} and x_{Sn} are calculated based on the individual uncertainties (inputs in the RSM software) for the relaxed in- and out-of-plane lattice parameters ($\Delta a_{\parallel,\perp,0}$ (Si, Ge, Sn)) and respective C13 and C33 (ΔC13, ΔC33 (Si, Ge, Sn)). Then, a set of 10 000 combinations referred as

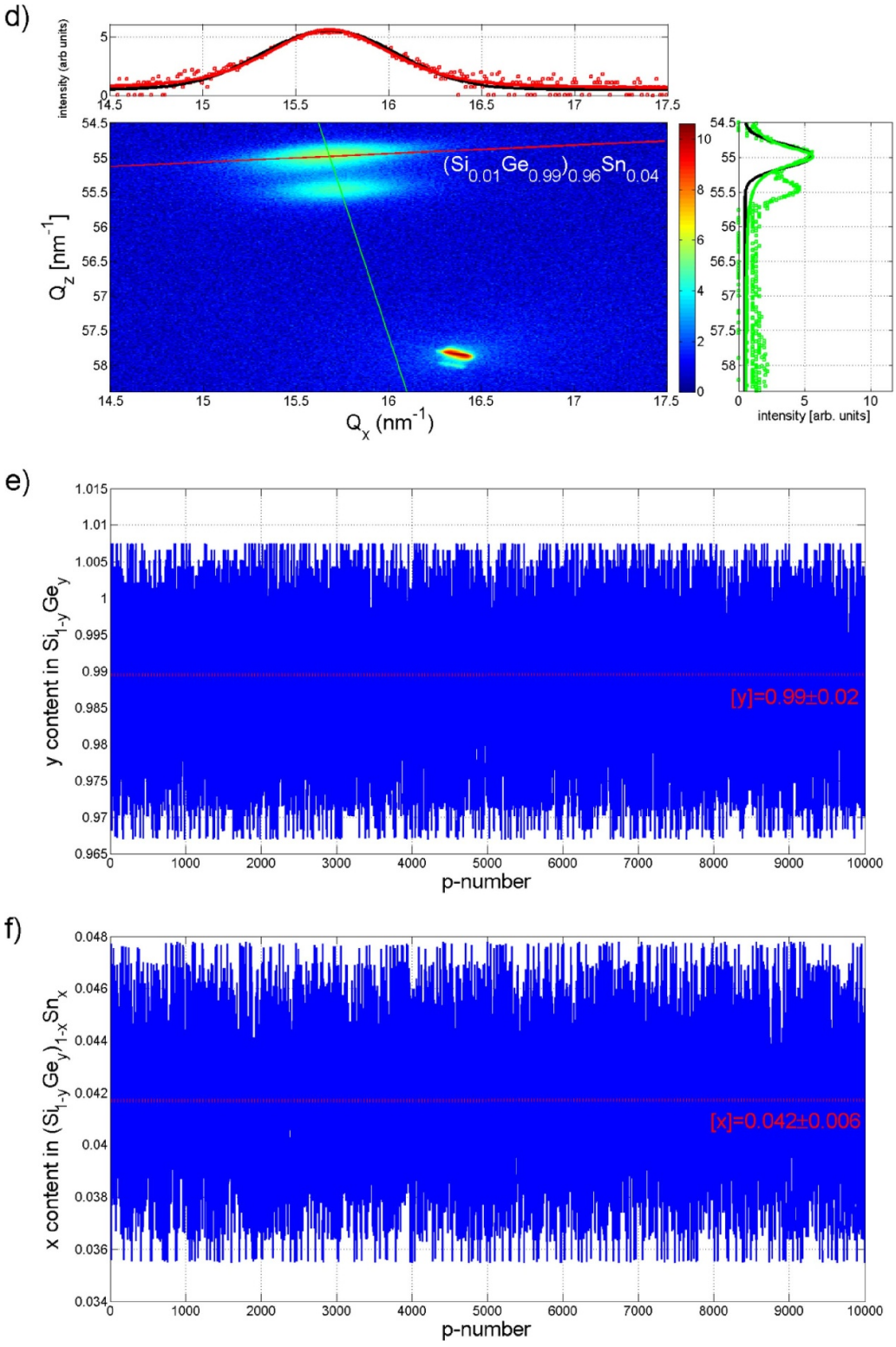

Figure 3. (Continued.)

p-numbers containing $a_{\parallel,\perp,0}$(Si, Ge, Sn) are generated through a Monte Carlo algorithm. Finally, the average and standard deviation of the y_{Ge} and x_{Sn} are determined. As an example, considering the eight free-variables present in the determination of x_{Sn} (4 in $a_{\parallel,\perp,0}$(Ge, Sn) and 4 in C13 (Ge, Sn) and C33 (Ge, Sn)) the effect of employing $a_{\parallel,\perp,0} \pm \Delta a_{\parallel,\perp,0}$ and C13(C33) $\pm$ ΔC13(C33) in the calculations of the Sn molar fractions results in 2^8 permutations which is considerable less than the 10 000 *p*-numbers generated. Therefore, the 10 000 *p*-numbers generated foresee high accuracy in the determination of the x_{Sn} molar fraction and high precision in the determination of the respective uncertainty. Figures 3(e) and (f) show

the derived y_{Ge} and x_{Sn} contents as function of the 10 000 p-numbers.

In each figure, the upper and right side one-dimensional plots show the experimental data along the specific red and green lines cuts depicted in the 2D plot. The green and red lines were determined using equation (1):

$$I(Q_{x,z}) = a_0 \times \left[(1-a_3) \times \exp\left(-\log(2) \times \left(\frac{(Q_x,Q_z) - Q_{\hat{x}},Q_{\hat{z}}}{\delta Q_{x,z}} \right)^2 \right) + \frac{a_3}{1+\left(\frac{(Q_x,Q_z) - Q_{\hat{x}},Q_{\hat{z}}}{\delta Q_{x,z}} \right)^2} \right]. \quad (1)$$

For a pure Gaussian, $a_3 = 0$, while $a_3 = 1$ corresponds to a pure Lorentzian, i.e. a_0 and a_3 are the simulated intensity and Lorentzian fraction, respectively. Screenshots of the *RSM software* highlighting the multi-step procedure described above are addressed in S1 by exemplifying the required parameters used to input in the file with respect to sample C4.

4. Experimental results and discussion

4.1. Study of the validity of the Vegard's rule of the $Ge_{1-x}Sn_x$ layers grown on Ge buffer layers and 100 Si substrates

The procedure summarized in section 3 is applied to the other three samples (C1 to C3). Representative reciprocal space maps around the 115 Si reciprocal lattice point evidencing the heteroepitaxial growth of Ge on the 100 Si substrate and the $Ge_{1-x}Sn_x$ binary on the Ge template are shown in figure 4. The fits of the experimental data using 2D-Gaussians is shown on the right side of each measured RSM. The horizontal dashed lines in the figure are included for guiding purposes and to emphasize the similarities between the 115 Si and 115 Ge buffer layer $Q_{\hat{z}}$ centres among the three samples. Furthermore, it allows evidencing the effect of the increase of the tin content, x_{Sn} (in $Ge_{1-x}Sn_x$), from samples C1 to C3.

The fits together with the experimental data corresponding to the RSM cuts are highlighted in figures 5(a)–(j)) for the four samples. Figures 5(a)–(i) correspond to the fits of the Si 115 Cu Kα_1, Si 115 Cu Kα_2, Ge and $Ge_{1-x}Sn_x$ projected against Q_x [100] direction while the figures 5(b)–(j)), correspond to the same cuts projected against Q_z [001] direction.

In figure 5, the cuts for each measured RSM are fitted and translated vertically for clarity. In the case of figures 5(g) and (h), the cuts in the vicinities of peak #4 (Ge layer), corresponding to samples C2 to C4, are represented while in figures 5(i) and (j), for sample C3 only one cut is performed in order to evidence/satisfy the observed splitting of the diffraction spot associated to the $Ge_{1-x}Sn_x$ binary (peaks #4 and #5). Moreover, the cuts around the 115 $Ge_{1-x}Sn_x$ of sample C1 are not included in the figures 5(g) and (h) due to the overlap between the Ge and the binary diffraction spots (peaks #3 and #4). The fits represented in red colour are executed using a PV function employing the optimized height, centre $\left(Q_{\hat{x}}^j, Q_{\hat{z}}^j\right)$, Gaussian width (by definition, twice of the full width at half maxima (FWHM)), and Lorentzian fraction outputs. The uncertainties of the derived PV coefficients are used to consider the lower and upper boundaries represented in green and blue colours, respectively. The good agreement between the experimental data and the PV fits along a given cut is evidenced in figure 5. In fact, as demonstrated in section 3, the fit using PVs satisfies better the experimental data than a pure Gaussian. In the executed fits, the Lorentzian fraction (a_3, equation (1)) is derived to be above 0.5. Moreover, figures 5(g) and (i) suggest similar inside the experimental and instrumental errors $\left(Q_{\hat{x}}^j,\right)$ centres for all j diffraction spots attributed to the $Ge_{1-x}Sn_x$ layer. On the other hand, the splitting of the diffraction spots with respect to [001] direction is evident from figures 5(h) and (j)) where the x_{Sn} content is shown in the inset. The centres and the full widths at half maxima derived for both orthogonal directions of the diffraction spots, ($Q_{\hat{x}}$, $Q_{\hat{z}}$) and ($\delta Q_{\hat{x}}$, $\delta Q_{\hat{z}}$), the in-plane and out-of-plane lattice parameters, $a^{||}$ and $a^{\perp}$, and germanium, y_{Ge}, and tin, x_{Sn}, contents together with the respective uncertainties for all samples are depicted in table 2. The mentioned relevant outputs are determined directly by fitting the cuts through the diffraction spots with PV functions.

According to table 2, for most of parameters derived from the Gaussian (not shown) and PV fittings, the absolute values determined for me former lie within the uncertainties derived for the latter.

The in- and out-of-plane lattice parameters were then determined using equations S3.2(a_1)–(b_1) and the deduced $(Q_{\hat{x}}, Q_{\hat{z}})$ co-ordinate pairs. The tin contents and respective uncertainties derived by the proposed method are: $x_{Sn,sample\ C1} = 0.009 \pm 0.007$, $x_{Sn,sample\ C2} = 0.017 \pm 0.005$, $x_{Sn,sample\ C3/Peak3} = 0.032 \pm 0.006$, $x_{Sn,sample\ C3/Peak4} = 0.043 \pm 0.004$ and $x_{Sn,sample\ C4} = 0.042 \pm 0.006$, respectively. The uncertainties are mainly affected by the determination of the peak centroid. In fact, according to equations S3.2(a) and (b) and error propagation theory, the uncertainty in the composition will be strongly affected by the uncertainties in the determination of the lattice parameters, which, in turn, is calculated from the $(Q_{\hat{x}}, Q_{\hat{z}})$ centroid peaks. Consequently, the $x_{Sn} = 0.009$ calculated for sample C1 presents the highest uncertainty (± 0.007) due to the fact of high level of peaks overlapping (115 $Ge_{0.991}Sn_{0.009}$ and 115 Ge). The uncertainties in the determination of the Sn content for the other samples vary between 0.004 and 0.007. To validate the method, the Sn content was determined by RBS and depicted in table 2, as also is the Sn content obtained by EDS. The experimental data of the RBS random spectra and respective simulations using the NDF code [41] are shown in figure 6(a) for samples C1, C2 and C4.

In figures 6(b)–(d), the energy interval between ~1700 and ~1950 keV of the RBS spectra is magnified in order to better visualize the differences between the random and aligned along the <001> axis spectra in the region close to the Sn-signal. Qualitatively, the sharp barriers depicted inset figure 6 is attributed to the chemical elements present in the sample (Si, Ge and Sn). The continuous line arrows refer to

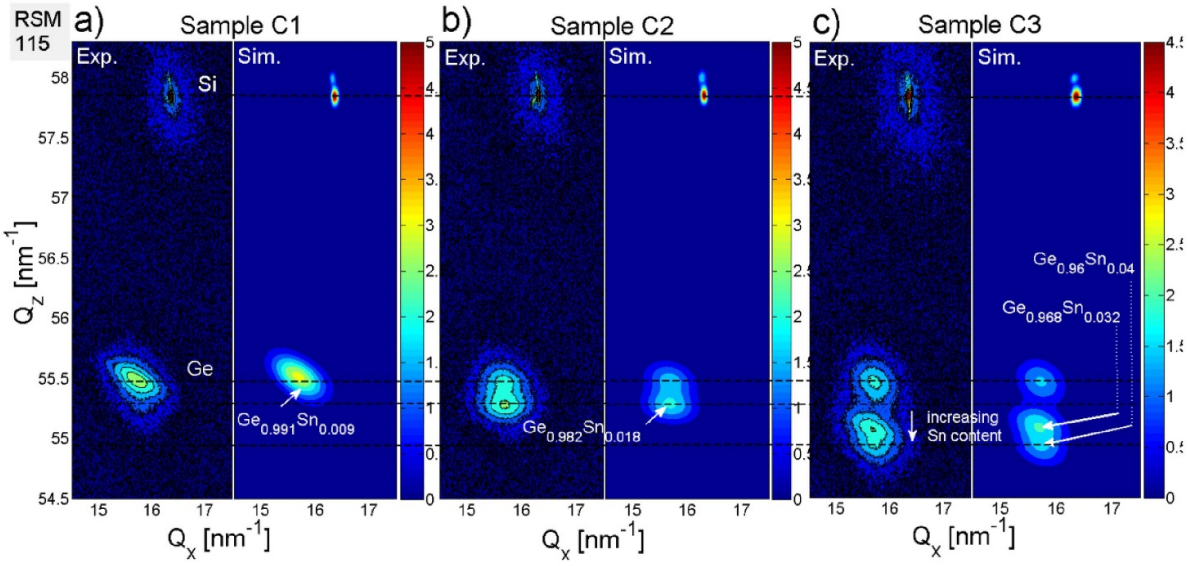

Figure 4. Comparison between the experimental RSMs in the vicinities of the 115 Si and simulations employing 2D Gaussians for 3 $Ge_{1-x}Sn_x$ binary layers grown on the Ge template and 100 Si substrate. The Si Cu Kα_2 centred on slightly higher $Q_{\tilde{z}}$ compared to the 115 Si Cu Kα_1 diffraction spots is also observed in all the three RSMs. $a^{||}$ and $a^{\perp}$ are inversely proportional to $Q_{\tilde{x}}$ and $Q_{\tilde{z}}$, respectively, showing increasing tin content from the left to the right side in the figure, i.e. from (a) to (c). Horizontal lines suggest the approximately the same $a^{\perp}$ for the three Si wafer pieces and also for Ge buffer in the three samples. The $Ge_{1-x}Sn_x$ layer is quasi-pseudomorphic with the respective Ge layer (both present approximately the same $Q_{\tilde{x}}$).

the chemical elements present at the surface (Ge, Sn and O) while the dashed line arrow refers to the energy of the element (Si) targeted by the $^4He^+$ and backscattered at a given depth according to the random spectra simulations. On the one hand, the Ge buffer layer thickness is directly proportional to ΔE_{Ge} illustrated in the random spectra of figure 6. On the other hand, the Sn-signal is partially overlapped with the Ge-signal, thus, complicating the quantification of the binary layer thickness. The increase of the tin content is clear from the increasing backscattering yield observed in the Sn-yield in figures 6(b)–(d). Inset are depicted the RBS derived Sn contents.

Although, as demonstrated in figures 6(a)–(d), very good qualities of the simulations are accomplished, several $Ge_{1-x}Sn_x$ layers with different composition and thicknesses are required to satisfy the experimental data. The dispersion at x_{Sn} among the simulated layers is below 0.2% while its respective thicknesses vary by 10 nm, evidencing, thus, the low level of measured composition heterogeneities and thickness fluctuations. In order to compare with the stoichiometry derived by RSM, a method based on the weighted x_{Sn} averaged along the total thickness of the $Ge_{1-x}Sn_x$ layer is applied. Specifically, $x_{Sn} = \frac{\sum_{j=1}^{N} x_{Sn}^{j} t^{j}}{\sum_{j=1}^{N} t^{j}}$ where x_{Sn}^{j} and t^{j} are the Sn contents and thicknesses of the individual (jth) layer, respectively. The Sn content derived via RBS for the 4 Sn-containing samples are 0.002, 0.017, 0.035 and 0.042. Uncertainties around 0.005 in x_{Sn} are suggested which agree with the ones found in literature, where the RBS manual analysis of $Al_{1-x}In_xN$/GaN layers is performed [52]. Therefore, the RBS derived x_{Sn} perfectly agrees with the ones derived via the XRD RSM counterpart. The estimation of the uncertainty in the determination of the tin content via the RBS is solely based upon graphical visualization of the obtained simulations using the NDF code [41]. Although the Sn content derived through both XRD and RBS techniques agree, it is of fundamental importance the procedure to calculate the uncertainties by the proposed method. Thus, no evidences of a deviation from Vegard's rule are found for the $Ge_{1-x}Sn_x$ system, within the Sn content range studied. Indeed, in most of the studies such deviations appear only for considerably larger values of x_{Sn}, of the order of 0.2 (see [53]). Furthermore, Xu *et al* suggested the low levels of accuracy if studies focussing the deviation from Vegard's rule are applied to highly strained $Ge_{1-x}Sn_x$ (and $Si_{1-y}Ge_y$) compounds (>1%) [54]. Therefore, it is fundamental to determine the level of strain in the different $Ge_{1-x}Sn_x$ layers studied here. Figure 7 shows the parallel ($\varepsilon_{||}$) and the perpendicular ($\varepsilon_{\perp}$) to the sample surface strains as function of the Sn content derived by XRD using either the two Sn contents derived for peaks #4 and #5 of sample C3 (figures 7(a) and (b)) and only the lower Sn content (peak #4) in figures 7(c) and (d). Inset figures 7(a)–(d)), the linear regression equation taking into account the uncertainties of the fitting parameters. It considers the Δx_{Sn}, $\Delta\varepsilon_{||}$, and $\Delta\varepsilon_{\perp}$. The fitting procedure involves a Monte Carlo algorithm to obtain the hyperbolic boundary curves. The uncertainty in the fitting parameters is computed in 5000 iterations, assuming that errors are Gaussian and centred. The upper and lower hyperbolic curves for both orthogonal deformations cross the relaxed Sn content at around zero Sn molar fraction for both situations depicted in figure 7. The Sn molar fraction used in figure 7 is the one derived through XRD. Nevertheless, the Sn contents derived by XRD and RBS are inside respective errors. The above behaviour suggests that the studied binary system does not require a correction for the

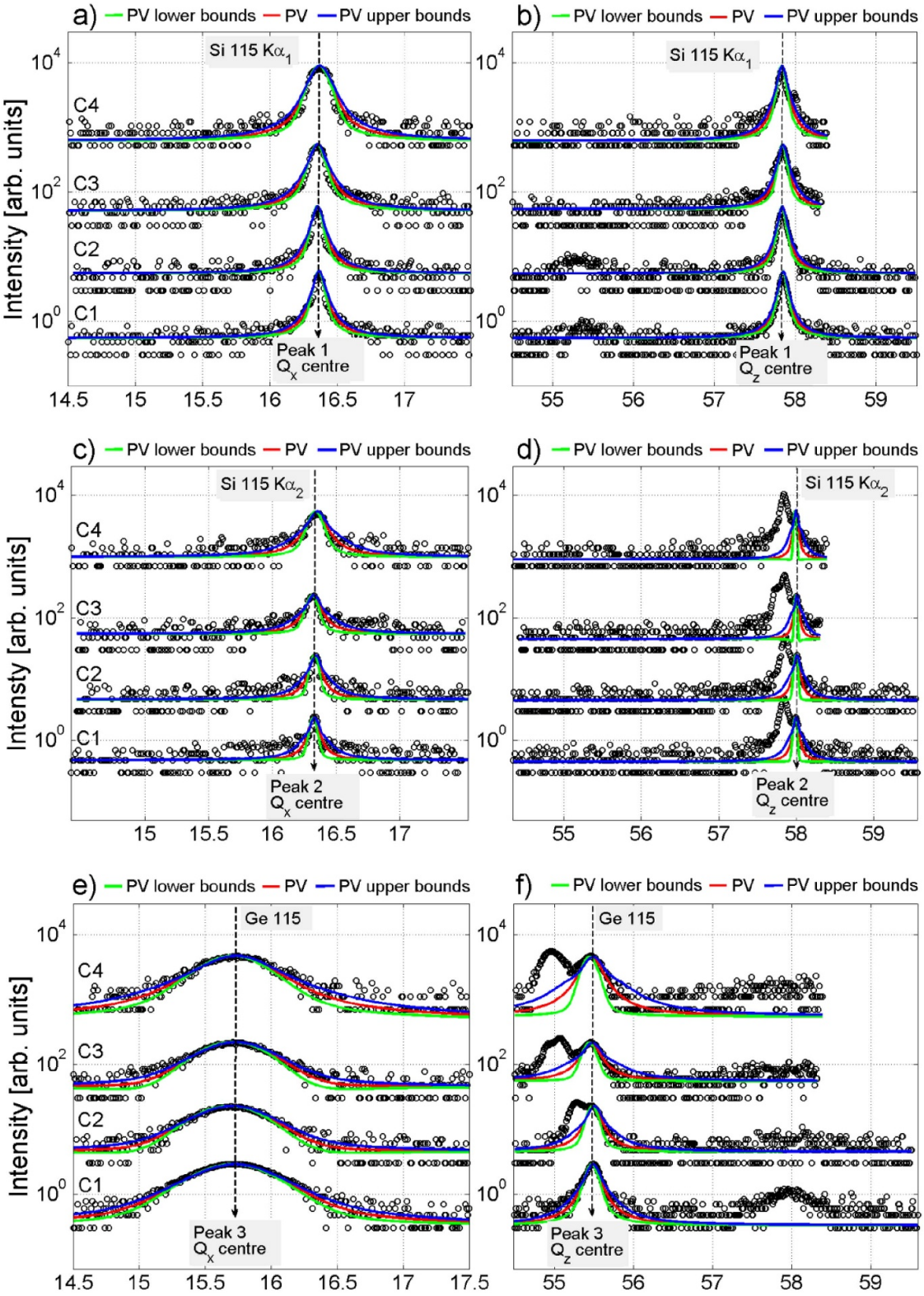

Figure 5. Cuts along the Q_x [100] direction, (a), (c), (e), (g) and (i), and Q_z [001] direction, (b), (d), (f), (h), (j)), respectively, of C1–C4 samples. The fits are performed using PVs by employing the coefficients (red curve) and the derived upper and lower boundaries (in blue and green curves, respectively). The black open circles correspond to the experimental data. Inset is indicated the 115 Ge peak of samples C1 to C4 and x_{Sn} content (in $Ge_{1-x}Sn_x$) of samples C2 to C4. Appropriate peak # assignment is illustrated.

Vegard's rule which is in agreement with the study reported in [54] for Sn contents up to 14%. The Si, Ge and Sn relaxed lattice parameters of 5.430 57, 5.656 92 and 6.489 31 Å used in [54] are inside the uncertainties employed in the calculations in this work (table 1). Although the above conclusion is supported considering the derived uncertainties, the

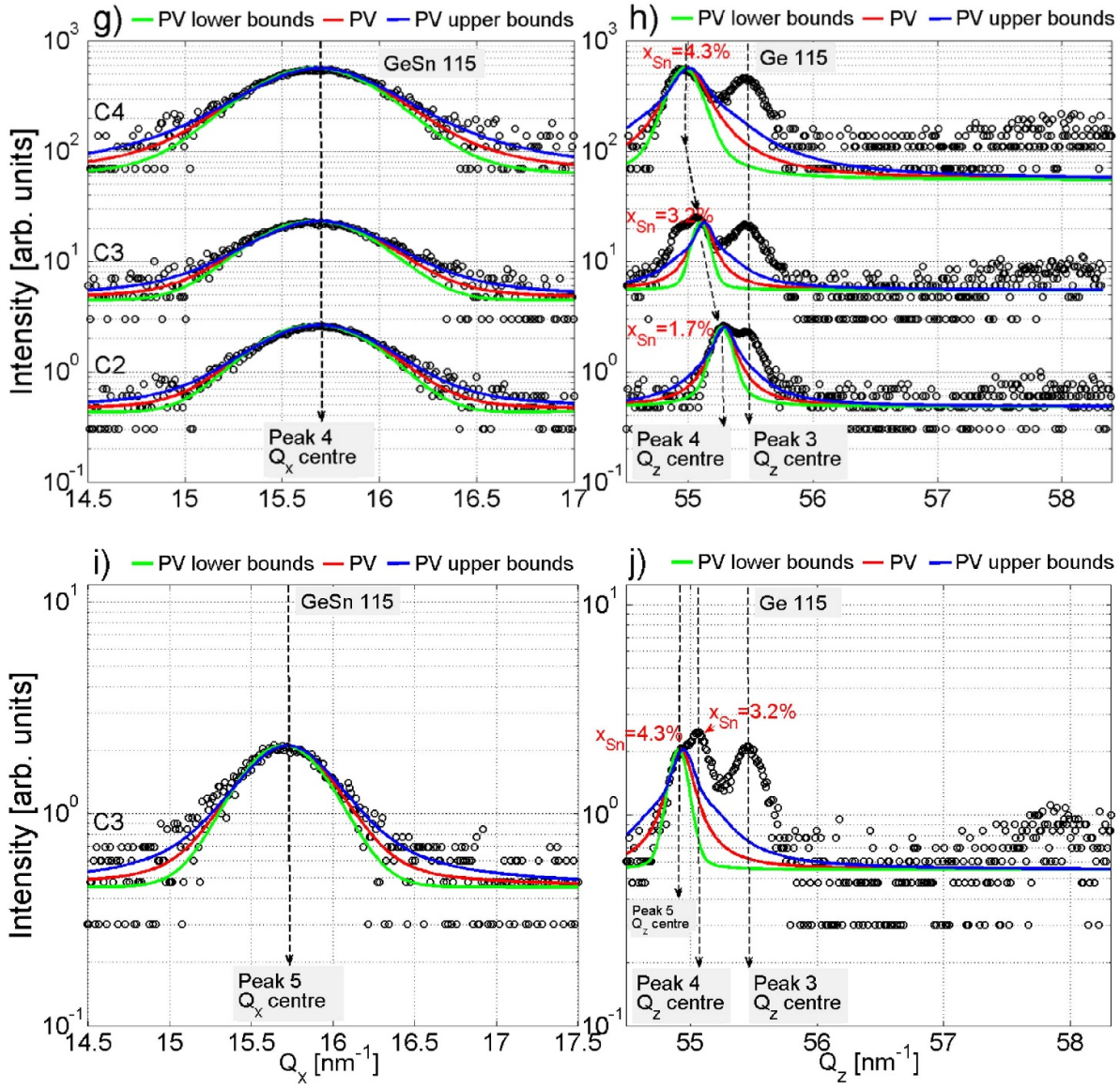

Figure 5. (Continued.)

y_0-ordinates contain high uncertainties. In fact, the y_0 ordinates and respective uncertainties depicted on top of each figure are $y_0 = 0.629\ 72 \pm 0.662\ 32$ and $y_0 = -0.4268 \pm 0.4838$ for samples C2 to C4 (figures 7(a) and (b)) considering in C3 the peaks #4 and #5 and $y_0 = 0.099\ 97 \pm 0.269\ 43$ and $y_0 = -0.1928 \pm 0.3352$ (figures 7(c) and (d)) considering only peak #4 in sample C3 and $\varepsilon_{\parallel}$ and $\varepsilon_{\perp}$, respectively. Sample C1 was removed from the above analysis due to the fact that the Sn content is too small and with same order as the respective uncertainty.

As illustrated in figure 7, the tin compounds studied, $\varepsilon_{\perp}$ and $\varepsilon_{\parallel}$ vary between -0.5% and 0.5%, respectively. Thus, nonlinear anharmonic contributions may be neglected in the frame of the elasticity theory. In the next section, the complex heteroepitaxy of the trilayer system and the influences of the compositional/strain heterogeneities, presence of impurities (oxygen), point defects and surface morphology on the $Ge_{1-x}Sn_x$ binary lattice parameters are discussed.

4.2. Discussion

The epitaxial relations between the 100 Si substrate and the Ge buffer layer as well as the latter with the $Ge_{1-x}Sn_x$, detailed in figure 8, are fundamental to understand what triggers the reduction of the crystalline quality of the binary with increasing tin content. In the inset in figure 8(a), the ($Q_{\hat{x}}$, $Q_{\hat{z}}$) reciprocal lattice units for the 115 relaxed Si, relaxed Ge are indicated with 'zero' subscript and the measured 115 $Ge_{1-x}Sn_x$ from C1 to C4 samples are indicated and represented with coloured symbols according to the nomenclature defined in figure 8(b). Furthermore, the relaxed ($Qx_{0,Sn}$,$Qz_{0,Sn}$) is calculated and plotted as a straight line marked ($R = 1$) in figure 8(a) for the entire compositional range ($0 \leqslant x_{Sn} \leqslant 1$). The relaxation line is calculated directly via the Vegard's rule as $a_{||,\perp Ge_{1-x}Sn_x} = a_{||,\perp,Ge}\ (1 - x_{Sn}) + a_{||,\perp,Sn} x_{Sn}$. Moreover, the vertical line, perpendicular to the Q_z units and passing through the 115 diffraction spot of the respective sample (different

Table 2. Centre coordinates, $(Q_{\hat{x}}, Q_{\hat{z}})$, FWHM along both orthogonal directions, $\delta Q_{\hat{x}}$ and $\delta Q_{\hat{z}}$, in- and out-of-plane lattice parameters, $a^{||}$ and $a^{\perp}$, and respective uncertainties derived from PVs fittings for samples C1 to C4. The composition of the compounds derived through XRD, RBS and EDS is also indicated.

Peak #		$Q_{\hat{x}}(\mathrm{nm}^{-1})$	$\delta Q_{\hat{x}}(\mathrm{nm}^{-1})$	$Q_{\hat{z}}(\mathrm{nm}^{-1})$	$\delta Q_{\hat{z}}(\mathrm{nm}^{-1})$	$a^{\|\|}$(Å)	$a^{\perp}$(Å)	Molar fraction
				Sample C1				
PV	1	16.3621 ± 0.0023	0.044 ± 0.003	57.8451 ± 0.0026	0.055 ± 0.004	5.4307 ± 0.0008	5.4310 ± 0.0002	—
	2	16.3254 ± 0.0059	0.042 ± 0.009	57.9891 ± 0.0078	0.036 ± 0.010	5.4429 ± 0.0019	5.4178 ± 0.0007	—
	3	15.7172 ± 0.0091	0.385 ± 0.012	55.4749 ± 0.0089	0.110 ± 0.012	5.6535 ± 0.0031	5.6631 ± 0.0009	1.004 ± 0.014
	4	15.6784 ± 0.0245	0.270 ± 0.026	55.4724 ± 0.0175	0.112 ± 0.018	5.6675 ± 0.0088	5.6633 ± 0.0018	0.009 ± 0.007
		x_{Sn} (RBS)	0.002 ± 0.005	x_{Sn} (EDS)	—	—	—	—
				Sample C2				
PV	1	16.3590 ± 0.0027	0.043 ± 0.003	57.8480 ± 0.0028	0.053 ± 0.004	5.4317 ± 0.0008	5.4308 ± 0.0003	—
	2	16.2742 ± 0.0060	0.045 ± 0.009	57.9990 ± 0.0083	0.038 ± 0.011	5.4600 ± 0.0021	5.4166 ± 0.0008	—
	3	15.6926 ± 0.0113	0.330 ± 0.015	55.4889 ± 0.0131	0.105 ± 0.017	5.6624 ± 0.0041	5.6617 ± 0.0013	1.018 ± 0.019
	4	15.6815 ± 0.0101	0.352 ± 0.013	55.2775 ± 0.0112	0.105 ± 0.015	5.6664 ± 0.0037	5.6833 ± 0.0011	0.017 ± 0.005
		x_{Sn} (RBS)	0.017 ± 0.005	x_{Sn} (EDS)	0.014	—	—	—
				Sample C3				
PV	1	16.3629 ± 0.0032	0.064 ± 0.004	57.8451 ± 0.0035	0.055 ± 0.005	5.4304 ± 0.0011	5.4311 ± 0.0003	—
	2	16.3177 ± 0.0072	0.061 ± 0.010	57.7999 ± 0.0075	0.027 ± 0.009	5.4455 ± 0.0024	5.4166 ± 0.0007	—
	3	15.7183 ± 0.0126	0.319 ± 0.015	55.4557 ± 0.0203	0.132 ± 0.031	5.6531 ± 0.0045	5.6650 ± 0.0021	1.009 ± 0.020
	4	15.6784 ± 0.0122	0.363 ± 0.016	55.1112 ± 0.0157	0.097 ± 0.021	5.6671 ± 0.0044	5.7005 ± 0.0016	0.032 ± 0.006
	5	15.7082 ± 0.0128	0.332 ± 0.018	54.9248 ± 0.0193	0.118 ± 0.028	5.6568 ± 0.0046	5.7198 ± 0.0020	0.040 ± 0.004
		x_{Sn} (RBS)	—	x_{Sn} (EDS)	0.034	—	—	—
				Sample C4				
PV	1	16.3588 ± 0.0039	0.088 ± 0.005	57.8453 ± 0.0035	0.057 ± 0.005	5.4318 ± 0.0013	5.4310 ± 0.0003	—
	2	16.3450 ± 0.0082	0.077 ± 0.011	57.9892 ± 0.0065	0.027 ± 0.009	5.4364 ± 0.0027	5.4178 ± 0.0006	—
	3	15.7214 ± 0.0125	0.330 ± 0.019	55.4625 ± 0.0225	0.154 ± 0.035	5.6520 ± 0.0045	5.6644 ± 0.0023	1.005 ± 0.020
	4	15.6791 ± 0.0131	0.396 ± 0.016	54.9857 ± 0.0193	0.176 ± 0.026	5.6673 ± 0.0041	5.7135 ± 0.0021	0.042 ± 0.006
		x_{Sn} (RBS)	0.042 ± 0.005	x_{Sn} (EDS)	0.028	—	—	—

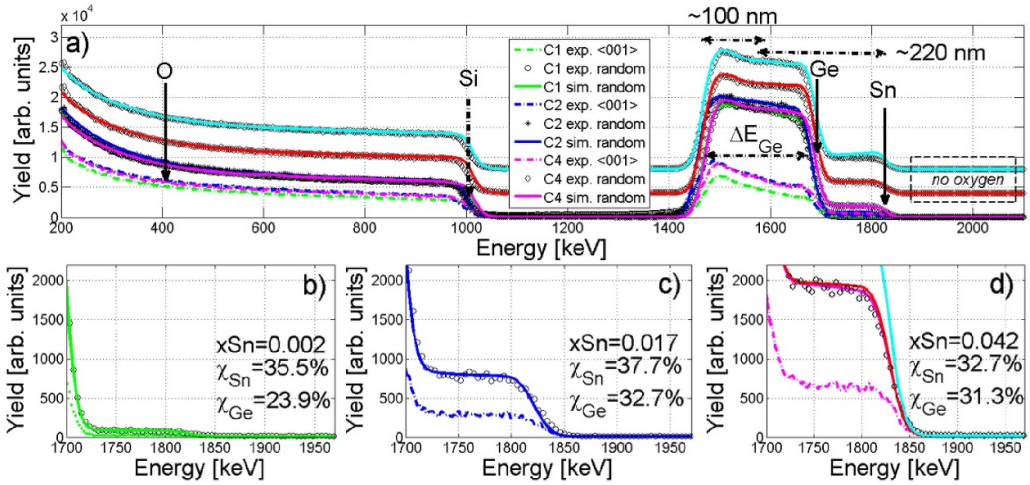

Figure 6. (a) RBS experimental random (symbols) and aligned along the <001> axis (dashed lines) spectra of C1, C2 and C4 samples. The measurements were performed using 2 MeV He^+ particles. The fits, illustrated with continuous lines, were executed using the NDF code [41]. The vertically translated experimental and fitted random spectra do not consider the presence of oxygen at the Ge buffer layer and $Ge_{0.958}Sn_{0.042}$ film, respectively. (b)–(d) Magnification of the spectra in the energy interval between ∼1700 and ∼1950 keV for better comparison between the <001> aligned and random spectra near the Sn barrier of the different samples.

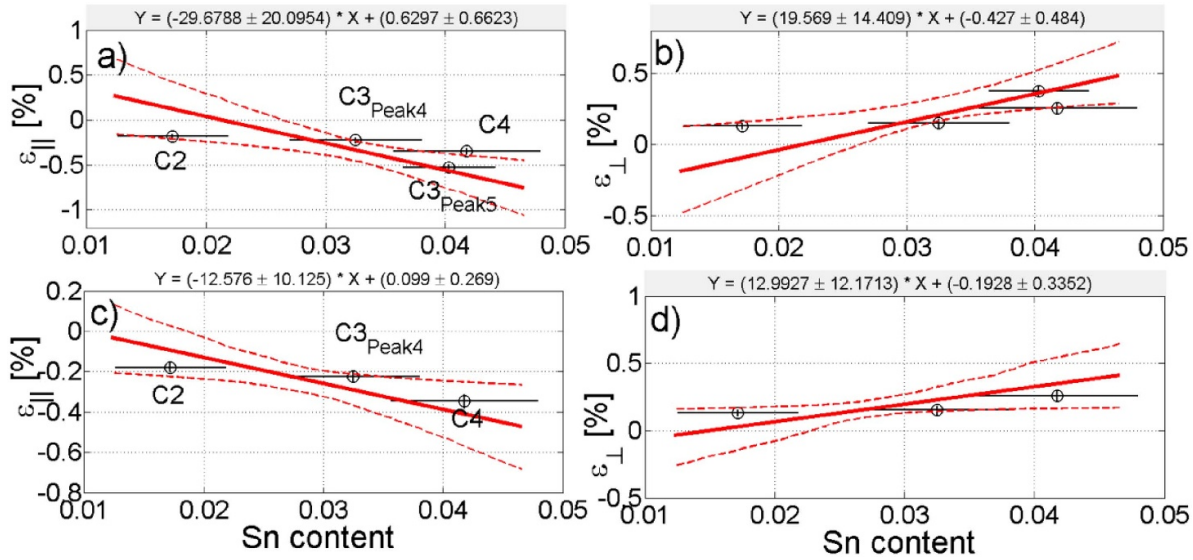

Figure 7. Parallel ($\varepsilon_{\parallel}$) (a), (c) and perpendicular ($\varepsilon_{\perp}$) (b), (d) deformation to the sample surface considering samples C2 to C4 where in C3 the double layer attributed to peaks #3 and #4 ($x_{Sn} = 0.032$ and $x_{Sn} = 0.04$) and only peak #3 ($x_{Sn} = 0.032$) is considered to linearize equation S3.3. The fits consider the uncertainties in the determination of the Sn content as well as in the measured and relaxed lattice parameters. Inset each image is the analytical equation derived from the Monte Carlo fitting method. Considering the derived lower and upper boundaries, the $Ge_{1-x}Sn_x$ cubic system does not require a correction to the Vegard's rule due to the fact that both orthogonal deformations show no strain when crossing at vanishing Sn content.

symbols) is designated as the pseudomorphic or the fully strained line ($R = 0$). The orthogonal lattice parameters of Si calculated for the four samples are quite similar and inside respective uncertainties as demonstrated in table 2 and figure 8(b). In fact, taking into consideration the uncertainty of 0.001 Å, $a_{\parallel,\perp}(\mathrm{Si}) = 5.431 \pm 0.001$ Å, all possible derived $(Qx_{\mathrm{Si,relaxed}}, Qz_{\mathrm{Si,relaxed}})$ pairs lie within the dashed-dot limiting circle centred on (16.3612, 57.8456) nm^{-1} (figure 8(b)). The 115 Si diffraction spot corresponding to sample C2 is centred at $(Q_{\hat{x}}, Q_{\hat{z}})_{\mathrm{Si}} = (16.359, 57.848)$ (table 2). A value of $a_{\perp}(\mathrm{Si}) = 5.4317$Å is deduced which almost matches the one from a relaxed Si bulk single crystal [55]. According to [56, 57] a thickness of 4 nm is enough to relax Ge on Si. Although, relaxed Ge is expected due to the nominal 100 nm thick Ge layer, strained Ge is measured for the four samples. The reason is attributed to the post-growing 330 °C annealing applied to the Ge layer in order to decrease the density of defects. Figure 8(c) refers to the representation in the reciprocal space of the involved diffraction spots from samples C2 (red colour circles) and C3 (green colour circles). The two $Ge_{1-x}Sn_x$ diffraction spots observed for sample C3 are perfectly distinguishable where the highest derived Sn content is

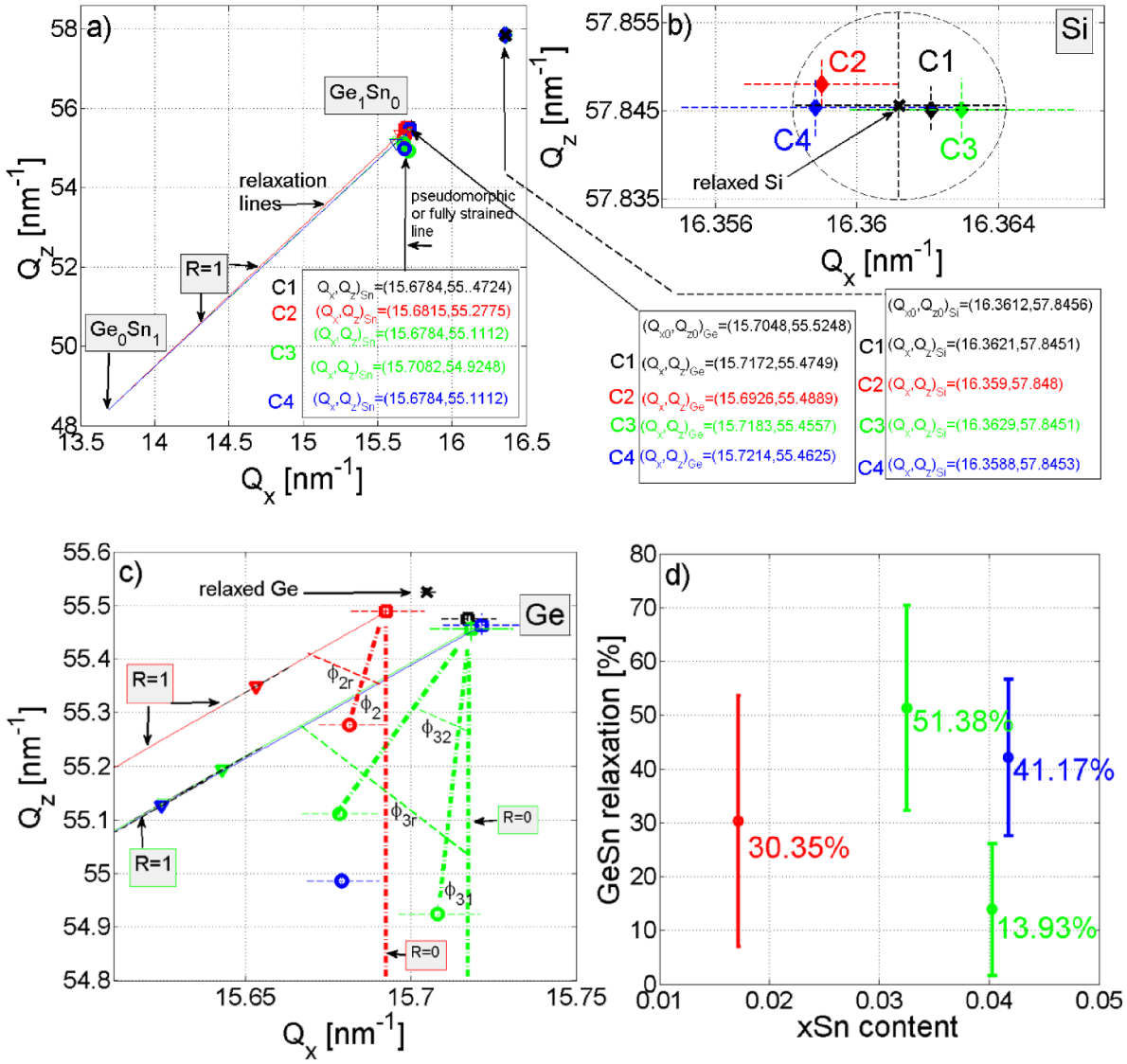

Figure 8. (a) Representation in the reciprocal space of the measured 115 Si, Ge, and $Ge_{1-x}Sn_x$ diffraction spots indicating the $R = 1$ theoretical relaxed $(Q_x, Q_z) = (Q_{x0,Si,Ge,Sn}, Q_{z0,Si,Ge,Sn})$ pair of co-ordinates for every x_{Sn} content from $x = 0$ (pure Ge) to Sn $= 1$ (pure Sn). (b) Magnification of the angular region (in the reciprocal region) attributed to the 115 Si diffraction spot illustrating with a dashed line circle the uncertainty of 0.001 Å in real-units and converted to reciprocal space units. The measured 115 Si diffraction spots from samples C1 to C4 lie inside the circle deduced for the relaxed Si. In the combined (a) and (b) all relevant (Q_x, Q_z) co-ordinate pairs for the individual diffraction spots are represented. (c) Representation in the reciprocal space of the magnification of (a) considering the angular region (in the reciprocal space) around the $Ge_{1-x}Sn_x$ for samples C2 and C3. $\phi_{2/3}$ and $\phi_{2r/3r}$ are the angles between pseudomorphic line for the 115 Ge buffer layer and the 115 $Ge_{1-x}Sn_x$ peak and the relaxed (Q_x, Q_z) calculated by the Vegard's rule for the given derived composition with respect to samples C2 and C3, respectively. (d) Relaxation degree and uncertainty calculated using $\phi_{2/3}$ and $\phi_{2r/3r}$, centroid peak positions and respective uncertainties.

attributed to the diffraction spot with lower Q_z (higher $a^{\perp}$). The pseudomorphic lines ($R = 0$), corresponding to fully strained material, are represented with dashed vertical lines connecting the 115 Ge diffraction spot and perpendicular to the $Q_z = 54.8$ nm^{-1} line. $\phi_{2/3}$ and $\phi_{2r/3r}$ refer to the angles between $R = 0$ and the measured 115 $Ge_{1-x}Sn_x$ peak and the corresponding relaxed $(Q_{\hat{x}}, Q_{\hat{z}})$ co-ordinates calculated using the Vegard's rule for the given derived composition with respect to samples C2 and C3, respectively. The triangles mark the $(Q_{\hat{x}}, Q_{\hat{z}})$ co-ordinates for the 100% relaxed layer with respect to the samples C2 (red) and C3 (green), respectively. The uncertainties in the lattice parameters of Ge and Sn are used to calculate the (Q_x, Q_z) interval indicated in figure by dashed lines close to the horizontal triangles. The $(Q_{\hat{x}}, Q_{\hat{z}})$ pair for relaxed Ge using the relaxed lattice parameters referred in [6] is also indicated.

A relaxation degree is clear for samples C2 and C3 because the line connecting the 115 Ge and the 115 $Ge_{1-x}Sn_x$ diffraction spots of each is not along $R = 1$ neither $R = 0$. The highest Sn content derived for sample C3 assigned previously to peak #5 lies closer to the pseudomorphic line rather than the one assigned to peak #4. Thus, for the former, higher strain

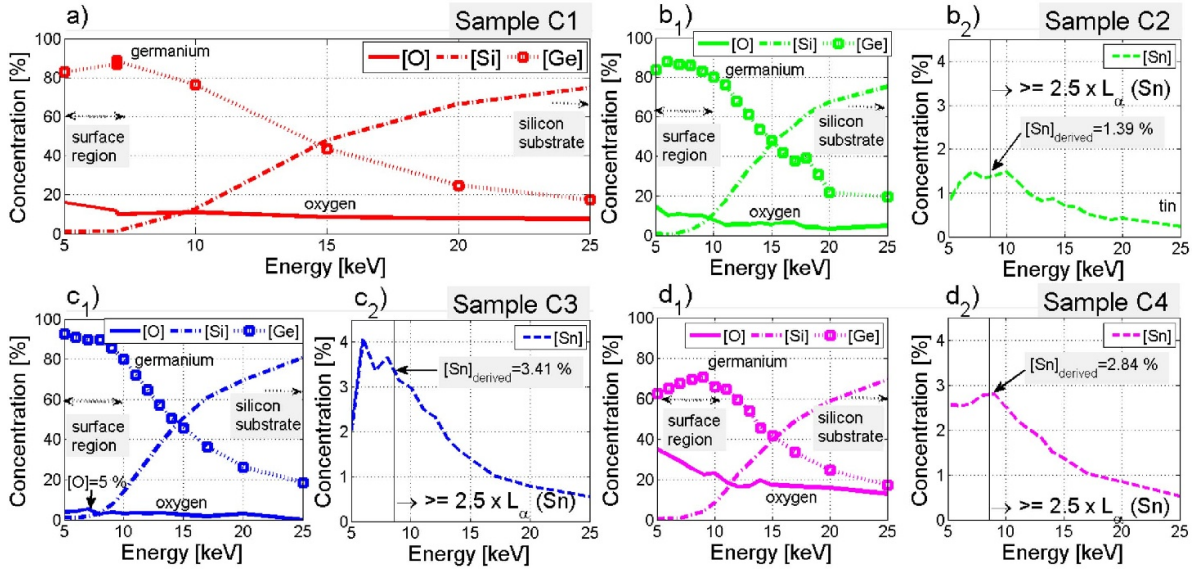

Figure 9. Evolution of the derived Si, Ge, O and Sn atomic percentages as function of the incident electron beam energy for samples C1, (a), C2, (b_{1-2}), C3, (c_{1-2}) and C4, (d_{1-2}), respectively.

is deduced while the latter presents higher levels of relaxation expressed in figure 8(d). The highest Sn content attributed to one of the $Ge_{1-x}Sn_x$ layers of sample C3 is almost fully strained (13.93% relaxed) while the other layers present much higher levels of relaxation (up to 51.38%). Therefore, considering all accounted uncertainties, peak #5 of sample C3 is the highest strained layer which corroborate with previous Raman studies [53]. Nevertheless, with the exception of the highest strain level assigned to peak #5 of sample C3 all the others present relaxation levels inside the uncertainties of each other. Specifically, the GeSn relaxation depicted in figure 8(b) takes into consideration the uncertainties in the Ge and Sn relaxed lattice parameters, respective stiffness coefficients, measured GeSn lattice parameters and chemical composition (table 2). The uncertainties in the Ge and GeSn lattice parameters are converted to Q_x and Q_z units using equation S3.2(a_{1-2}) and evidenced in figure 8(c) with horizontal and vertical dashed lines, respectively. Therefore, the relaxation degree may be determined as the angle between the $Ge_{1-x}Sn_x$ $(Q_{\hat{x}}, Q_{\hat{z}})$ diffraction spot and the $R = 1$ or $R = 0$ lines. Using sample C2 as an example, if ϕ_2 would be equal to ϕ_{2r} (see figure 8(c)) then the compound would be fully relaxed. In reality, ϕ_2 is approximately 1/3 of ϕ_{2r} resulting in a relaxation degree of ∼30%. Furthermore, as the uncertainties in table 2 are $(\Delta Q_{\hat{x}}, \Delta Q_{\hat{z}})_{Ge} = (0.0113, 0.0131)$ nm^{-1}, $(\Delta Q_{\hat{x}}, \Delta Q_{\hat{z}})_{Ge0.983Sn0.017} = (0.0101, 0.0112)$ nm^{-1}, the strain ranges between ∼5% and ∼55% as a result of the dispersion in ϕ_2 caused by the calculated uncertainties in compound reciprocal lattice units. A Monte Carlo algorithm generates 30 000 combinations of different $(Q_{\hat{x}} \pm \Delta Q_{\hat{x}}, Q_{\hat{z}} \pm Q_{\hat{z}})_{Ge/Ge0.983Sn0.017}$ and calculates the relaxation degree of each combination. The absolute value depicted in figure 8(c) matches with the calculated average strain while the uncertainty corresponds to the standard deviation.

What is more, the high dispersion for the relaxation of the compound may be concluded geometrically from figure 8(c) by connecting the $Q_{\hat{x}} + Q_{\hat{x}}$ for Ge with the $Q_{\hat{x}} - Q_{\hat{x}}$ for GeSn reciprocal lattice point defined. It is clear from figure 8(d) that taking into account the above uncertainties, the strain magnitude calculated for the GeSn layer of sample C2 ($30 \pm 23\%$) is impossible to be distinguished from the strain calculated for the GeSn layer of sample C4 ($41 \pm 15\%$) neither the same for the highest Sn content layer from sample C3 ($14 \pm 12\%$). In fact, according the derived uncertainties, the only conclusion possible is the different strain states for the two different chemical compositions GeSn layers found for sample C3, where the strain derived for the lowest Sn content strained layer is $51 \pm 19\%$ while for the highest Sn content, the strain magnitude is found to be $14 \pm 12\%$. Therefore, further attention is required in the quantification of the density of dislocations as extended defects are Burgers vector and lattice parameters magnitude' dependent. The presence of impurities, e.g. oxygen, point and interstitial defects and the surface morphology were investigated through EDS/scanning electron microscopy (SEM)/atomic force microscopy (AFM), XRD/XRR and ion channelling. Figure 9 shows the Si, Ge, O and Sn atomic percentages as functions of the incident electron beam energy for samples (C1, a), (C2, b_{1-2}), (C3, c_{1-2}) and (C4, d_{1-2}), respectively. The EDS spectra for samples C1 to C4 and from where the area calculated for the individual chemical element divided by the area of the total spectrum are shown in S4. Inset is the derived Sn contents for samples C2 to C4. According to figure 9, there is no sufficient statistics to infer a Sn molar fraction with respect to sample C1. The vertical lines depicted in figures 9(b_2), (c_2) and (d_2) refer to the minimum of energy required to satisfy the condition of being equal of greater than two and half times the tin L_α transition used for chemical quantification. The surface region (energies below 10 keV) and the direction towards the substrate is also inset each sub-figure. Sn

contents of 1.39%, 3.41% and 2.84% are found for samples C2, C3 and C4, respectively. The Sn content derived via EDS data lies inside the uncertainties for samples C2 and C3 but in the case of sample C4, it is below the value derived by the other techniques. One possible reason is the oxygen over-stoichiometry found in sample C4 reaching almost 40% at the surface and lowering to 20% of atomic percentages in the energy range appropriate to probe the $Ge_{1-x}Sn_x$ layer (8.6 keV marked in figure 9(d_2)).

The presence of oxygen may induce higher lattice parameters, thus higher derived Sn contents. The spectra represented in red and cyan in figures 6(a) and (d) and marked with a dashed line rectangle show the simulation of the random spectra from sample C4 without assuming no oxygen in the double $Ge_{0.958}Sn_{0.042}$ and Ge buffer layers. By not considering the oxygen in the layers, the edge barrier of the Ge from the surface and buffer layers-signal is not well simulated while the Sn-signal has no impact in its yield. In order to compensate the difference in the Ge-signal without including oxygen, more Sn is required. The effect is shown in the simulated spectra represented in cyan. In fact, the Ge edge-signal is now correctly simulated at the expenses of a worst quality simulation with respect to the Sn-signal. With respect to the RBS analysis, the source of misinterpretation is attributed to the fact that oxygen, being a light chemical element, thus with small Rutherford backscattering cross-section at 2 MeV and $^4He^+$ particles does not have a significant effect in overall the spectra. Nevertheless, higher concentration of oxygen was found at C4 where an average of 6.17% is deduced from the simulations of the RBS spectra (figure 6(d)). On the other hand, C1, C2 and C3 reveal, by RBS, lower concentrations of oxygen, i.e. 3.5%, 4.4% and 1.8%, respectively. Also interesting to note is the fact that the sample C3 with oxygen levels of 5% found via EDS (marked in figure 9(c_1)) is the sample where the two $Ge_{1-x}Sn_x$ layers with slightly different compositions were assigned. One of the $Ge_{1-x}Sn_x$ layers, specifically, the one assigned to peak #5 in figures 5(h) and (i) reveals the highest level of strain ($R = 13.53\%$, figure 8(d)). The pseudomorphic degree is then related to the oxygen impurity concentration. To minimize the concentration of the oxygen in the Ge layer, found to be capped by a thin oxide layer, an iterative procedure of dislodging by dipping in hydrofluoric acid was followed in tin-compounds grown by low temperature magnetron sputtering [58]. In the case of the MBE GeSn layers described here only an annealing treatment was executed to prevent the tin aggregation and/or segregation. Moreover, the Ge layer thicknesses were around 100 nm, i.e. thinner than usual CVD or magnetron sputtering grown Ge templates of no less than 250 nm [58–60]. The crystalline quality of the binaries, and in particular concerning the presence of point defects, was assessed and tentatively correlated with the complex heteroepitaxial growth of the binary on the Ge virtual substrates. The total thickness derived by x-rays (detailed analysis of the simulations is addressed in S5) and ion beams agree perfectly with the one observed by BSE after chemical elements analysis of 284 ± 27 nm. In the simulations was used the static DW factor, i.e. DW = 0 for perfect single crystal and DW = 1 for amorphous-like structure. The static DW factor is averaged to be 0.32 ± 0.04 for the $Ge_{1-x}Sn_x$ binaries showing the reasonable good crystalline quality of layers. The standard deviation suggests low level of crystalline quality heterogeneity with depth. To further access the crystalline quality and in particular the deviation from the regular lattice sites, i.e. point/interstitial defects, aligned spectra along the <100> axis were also accumulated (figures 6(a)–(d)). The minimum yield (χ_{min}) depicted inset (figures 6(b)–(d)) is the ratio between the yield in the aligned spectrum to that of the random RBS range from 20% to 40% for the binary layers indicating a reasonable good and homogeneous crystal quality. Thus, the derived crystalline quality for the binary using x-rays and ion beam techniques agree. The minimum yield found for the Ge layers is slightly lower showing its better crystalline quality if compared to the same quantity derived for the binary layers. Finally, the surface morphology is explored by XRR. The XRR patterns and respective simulations and fittings are shown in figure 9(a). The simulations were performed using the MROX code following the dynamical theory recursive method developed by Parratt [61]. Furthermore, due to the impossibility of obtaining a reasonable fit considering homogeneous $Ge_{1-x}Sn_x$ layers, a function to estimate the contribution of pores using the kinematical model developed by Maaze *et al* [62] was included. The contribution of the pores in the XRR scans is visible around 1.5° where a small shoulder suggests the small-angle x-ray scattering due to the randomly dispersed pores in the surface tin film. Clear improvement of the fitting was possible by considering the contribution of pores and the derived thickness matches with the ones observed by SEM, and simulated by RBS and XRD. For the simulations, and to estimate the density, pores with spherical shape and an averaged inter-distance between 10 nm and 1 μm are assumed. The fits were performed using a standard genetic algorithm and are presented in figure 10(a). A density of around 7 g cm^{-3} was obtained for the surface layers, which is in the same level of the one obtained by RBS and lower than the bulk density of Sn (7.3 g cm^{-3}). Furthermore, according to figure 10(b) and inset figure 10(a) the derived density decreases as a function of depth and presents close nominal densities of Ge (5.3 g cm^{-3}) around 200 nm. The higher density slightly below the value for bulk Sn deduced for the first 20 nm depicted in red colour in figure 10(b) suggests the presence of metallic clusters. In particular, sample C3 results show typical behaviour associated to Sn segregation/precipitation, where the GeSn film structure is composed of two regions with different Sn contents [63]. In fact, the derived averaged density for sample C3 (green curve in figure 10(b)) in the first 100 nm is higher than for samples C1 and C2. The segregation and/or precipitation mechanisms are expected due to the low solubility of Sn in Ge and the larger size of Sn atoms. Furthermore, depending on the Sn content the first 50–100 nm grown GeSn usually has a 0.5%–1% lower Sn content due to the fact that it grows lattice match to Ge, thus, under high strain. The derived density is also an indication of an oxygen over-stoichiometry at the surface, as RBS suggested. Moreover, the XRR derived roughness's shown in figure 10(c) agree with the ones observed by AFM (not shown). Moreover, the high rough GeSn layers may be attributed to the segregation phenomena or to the presence of pyramids type defects. In fact, to high quality chemical

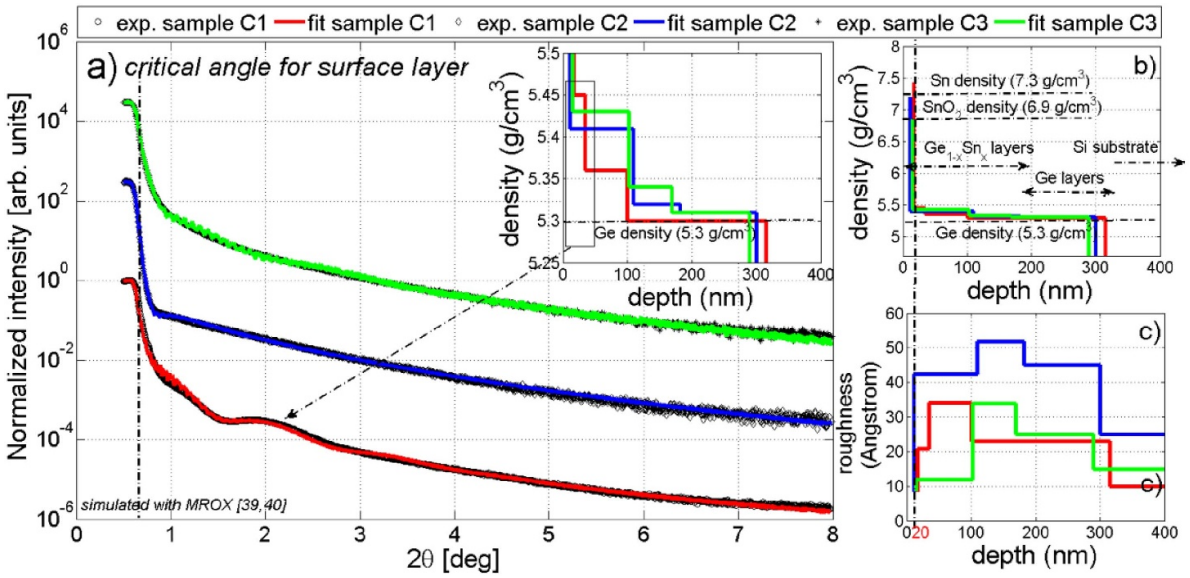

Figure 10. (a) C1, C2 and C3 experimental and simulations of the XRR specular scans in the vicinity of the 000 reflection (surface) showing with the vertical dashed line that the density at the surface is relatively the same in the three samples. The fits were performed using the MROX code [39, 40]. Inset is the magnification of the density (in g cm^{-3}) as function of depth (in the region of interest of $Ge_{1-x}Sn_x$ + Ge). (b) Density as function of depth output from the simulations shown in (a). (c) Roughness (in Å) of the different layers used in the XRR simulations.

vapour deposition (CVD) grown GeSn, the surface roughness is expected not to exceed 1 nm [63] while on the MBE layers studied here, the surface roughness easily reach twice of that value. GeSn compound grown by CVD usually shows better uniformity and crystalline quality than that by MBE [64]. Although, high quality MBE GeSn layers have been reported, the studies focus low tin content compounds [8, 12, 30, 31]. It is interesting to note that depending on the gases and the growing techniques, particular kind of defects may be created which may drive segregation. For example, Ge_2H_6 as well as well as $SnCl_4$ as being used as precursors in the CVD of high-quality GeSn with Sn compositions up to ∼13% [65]. The defects, on the other hand, are required to relax the lattice further motivated by the lack of appropriate substrate, i.e. with less lattice mismatch with respect to the tin-compound. The sizes of Ge and Sn atoms induces an elevated number of point defects which agrees with the high minimum yield derived from the ion channelling measurements and the low DW from the simulations of the 004 2θ–ω scans.

Therefore, the deviation from pseumodorphic $Ge_{1-x}Sn_x$ on the Ge layers, observed compositional/strain heterogeneities along the growing direction, measurable phase separation in the binary, interstitial and/or point defects accumulation in the cubic surface bi-layer crystalline structure, interface roughness's reaching the nanometre scale do not contribute to a deviation of the Vegard's rule in the low tin germanium content (<5%) system.

5. Conclusions

The ∼200 nm thick $Ge_{1-x}Sn_x$ epilayers stacked on ∼100 nm Ge buffer layers and Si 100 substrates were successively grown by MBE. The tin contents were derived by new XRD RSM software. The software fits the asymmetric 115 reciprocal lattice point using 2D-Gaussians and refines the solution by means of PVs functions for the cuts along orthogonal directions calculated for the rotation of the different diffraction spots. Sn contents of 0.009 ± 0.007, 0.017 ± 0.005, double layer containing 0.032 ± 0.006 and 0.040 ± 0.004 and 0.042 ± 0.006 for samples C1, C2, C3 and C4 are derived. The high uncertainty derived for the Sn content in sample C1 is a consequence of the partial 115 diffraction spot overlapping between the binary and the Ge buffer layer. Vegard's rule was tested for the $Ge_{1-x}Sn_x$ cubic system by comparing the Sn contents derived through XRD and RBS. With respect to the latter, Sn contents of 0.002, 0.017, 0.035 and 0.042 were obtained with uncertainties of 0.005 estimated by direct observation of its effect in the spectra. Within the derived uncertainties, a linear relation between the single chemical elements representing the binary is sufficient. Thus, within the compositional range studied no evidences of soliciting a correction are found. The complex heteroepitaxial growth is ascertained from the dispersion of the relaxation degrees found for the individual samples. While the highest Sn content found for sample C4, i.e. $Ge_{0.968}Sn_{0.042}$, and the lowest Sn content derived for one of the layers of sample C3 ($Ge_{0.958}Sn_{0.032}$) present degrees of relaxation of 41.17% and 51.38%, the highest Sn content layer of sample C3 grew almost pseudomorphic with the Ge buffer layer. Moreover, the binary layer with the second highest Sn content (C2) is 30.35% relaxed. Complex mechanisms triggering composition/strain heterogeneities are found. In particular, phase separation reaching 0.8% is observed for sample C3 (0.032), while variations up to 0.6% and 0.2% of Sn content with depth are simulated by XRD and RBS, respectively. Furthermore, point defects,

oxygen-rich regions, Sn segregation and surface morphology are found to constitute limitations to the Sn solubility within the ∼200 nm germanium tin films. With respect to the former, Debye Waller factors of 0.3 and minimum yields between 0.3 and 0.4 are found. Ion channelling complements point/interstitial defects analysis showing Sn to be slightly more deviated from the regular lattices sites if compared to Ge. Therefore, the Ge layers are slightly crystalline quality enhanced if compared to the $Ge_{1-x}Sn_x$ surface layers. The samples are not oxygen-free. Sample C3 revealed the lowest amount of oxygen compared to the other three samples. What is more, the most strained layer is observed for the highest Sn content layer of sample C3 suggesting strain relaxation of the lattice due to the oxygen impurities in samples C1, C2 and C4. Densities close to pure Sn (white tin 7.26 g cm^{-3} and grey tin 5.75 g cm^{-3}) at the surface decreasing its magnitude towards the border of the ∼200 nm tin film are calculated through the simulation of the XRR measurements. The simulations also suggest the presence of metallic Sn clusters at the surface. The Sn clusters and oxygen rich regions may induce the high average roughness of above 4 nm as obtained for the surface. The presented work demonstrates the single crystalline properties of the $Ge_{1-x}Sn_x$ compounds revealing that the incorporation of Sn, even for low Sn contents, is a tough technological task. Breaking the limited solubility Sn in Ge is, thus, fundamental to develop Si-compatible direct band gap material with controlled lattice parameters and band gap energy crucial for optoelectronic and microelectronic devices in the near infrared region.

Data availability statement

The data that support the findings of this study are available upon reasonable request from the authors.

Acknowledgments

This work was supported by the Portuguese Foundation for Science and Technology (FCT) in the framework of the Pluriannual Strategic Funding UID/FIS/50010/2019. F O acknowledges the FCT PhD Grant and thanks the Institut für Halbleitertechnik, Universität Stuttgart for hospitality. The authors acknowledge Professor J Schulze for providing the MBE facilities and the growing of the growing of the germanium tin films.

ORCID iDs

S Magalhães https://orcid.org/0000-0002-5858-549X
E Alves https://orcid.org/0000-0003-0633-8937

References

[1] Bauer M, Taraci J, Tolle J, Chizmeshya A V G, Zollner S, Smith D J, Menendez J, Changwu H and Kouvetakis J 2002 Ge-Sn semiconductors for band-gap and lattice engineering *Appl. Phys. Lett.* **81** 2992
[2] Kouvetakis J, Menéndez J and Chizmeshya A V G 2006 Tin-based group IV semiconductors: new platforms for opto-and microelectronics in silicon *Ann. Rev. Mater. Res.* **36** 497
[3] Chibane Y and Ferhat M 2010 Electronic structure of Sn_xGe_{1-x} alloys for small Sn compositions: unusual structural and electronic properties *Appl. Phys.* **107** 053512
[4] Pulikkotil J J, Chroneos A and Schwingenschlögl U 2011 Structure of Sn_xGe_{1-x} random alloys as obtained from the coherent potential approximation *J. Appl. Phys.* **110** 036105
[5] Gupta S, Köpe B M, Nishi Y and Saraswat K C 2013 Achieving direct band gap in germanium through integration of Sn alloying and external strain *J. Appl. Phys.* **113** 073707
[6] Bhargava N, Coppinger M, Prakash Gupta J, Wielunski L and Kolodzey J 2013 Lattice constant and substitutional composition of GeSn alloys grown by molecular beam epitaxy *Appl. Phys. Lett.* **103** 041908
[7] Ventura C I, Querales-Flores J D, Fuhr J D and Barrio R A 2013 Electronic structure of $Ge_{1-x-y}Si_xSn_y$ ternary alloys for multijunction solar cells *Prog. Photovolt., Res. Appl.* **21** 112
[8] Kasper E, Kittler M, Oehme M and Arguirov T 2013 Germanium tin: silicon photonics toward the mid-infrared *Photon. Res.* **1** 69
[9] Tonkikh A A, Eisenschmidt C, Talalaev V G, Zakharov N D, Schilling J, Schmidt G and Werner P 2013 Pseudomorphic GeSn/Ge (001) quantum wells: examining indirect band gap bowing *Appl. Phys. Lett.* **103** 032106
[10] Oliveira F, Fischer I A, Benedetti A, Zaumseil P, Cerqueira M F, Vasilevskiy M I, Stefanov S, Chuissi S and Schulze J 2015 Fabrication of GeSn-multiple quantum wells by overgrowth of Sn on Ge by molecular beam epitaxy *Appl. Phys. Lett.* **107** 262102
[11] Tsukamoto T, Hirose N, Kasamatsu A, Mimura T, Matsui T and Suda Y 2015 Investigation of Sn surface segregation during GeSn epitaxial growth by Auger electron spectroscopy and energy dispersive x-ray spectroscopy *Appl. Phys. Lett.* **106** 052103
[12] Kormoš L, Kratzer M, Kostecki K, Oehme M, Sikola T, Kasper E, Schulze J and Teichert C 2017 Surface analysis of epitaxially grown GeSn alloys with Sn contents between 15% and 18% *Surf. Interface Anal.* **49** 297–302
[13] Fewster P F 2003 *X-ray Scattering from Semiconductors* 2nd edn (London: Imperial College Press)
[14] Magalhães S *et al* 2015 Composition, structure and morphology of $Al_{1-x}In_xN$ thin films grown on $Al_{1-y}Ga_yN$ templates with different GaN contents *J. Phys. D: Appl. Phys.* **48** 015103
[15] Magalhães S *et al* 2017 Validity of Vegard's rule for $Al_{1-x}In_xN$ (0.08<x<0.28) thin films grown on GaN templates *J. Phys. D: Appl. Phys.* **50** 20
[16] Lorenz K *et al* 2010 $Al_{1-x}In_xN$/GaN bilayers: structure, morphology and optical properties *Phys. Status Solidi* b **247** 1740–6
[17] Peres M, Magalhães S, Soares M R, Soares M J, Rino L, Alves E, Lorenz K, Correia M R, Lourenço A C and Monteiro T 2013 Disorder induced violet/blue luminescence in rf-deposited ZnO films *Phys. Status Solidi* c **10** 662–6
[18] Magalhães S, Peres M, Fellmann V, Daudin B, Neves A J, Alves E, Monteiro T and Lorenz K 2010 Functionalizing self-assembled GaN quantum dots superlattices by Eu-implantation *Appl. Phys.* **108** 084306
[19] D'Costa V, Fang Y-Y, Tolle J, Kouvetakis J and Menendez J 2010 Ternary GeSiSn alloys: new opportunities for strain

and band gap engineering using group-IV semiconductors *Thin Solid Films* **518** 2531
[20] Wendav T, Fischer I A, Montanari M, Soellner M H, Klesse W, Capellini G, von den Driesch N, Buca D, Busch K and Schulze J 2016 Compositional dependence of the band-gap of $Ge_{1-x-y}Si_xSn_y$ alloys *J. Appl. Phys. Lett.* **108** 242104
[21] Chizmeshya A V G, Bauer M R and Kouvetakis J 2003 Experimental and theoretical study of deviations from Vegard's rule in the Sn_xGe_{1-x} system *Chem. Mater.* **15** 2511–9
[22] Baroni S, de Gironcoli S and Giannozzi P 1992 Structure and thermodynamics of SiGe alloys from computational alchemy *Structural and Phase Stability of Alloys* ed J L Morán-López, F Mejía-Lira and J M Sanchez (Boston, MA: Springer) p 134
[23] Mesli A, Vl K L, Nylandsted Larsen D A and Abrosimov N V 2006 Defects and impurities in SiGe: the effect of alloying *Nucl. Instrum. Phys. Res.* B **253** 154–61
[24] Sudhir G S, Peyrot Y, Krüger J, Kim Y, Klockenbrink R, Kisielowski C, Rubin M D, Weber E R, Kriegseis W and Meyer B K 2011 Effect of Mg, Zn, Si, and O on the lattice constant of gallium nitride thin films *MRS Online Proc. Libr.* **482** 525
[25] Muromura T 1982 Effect of oxygen and carbon impurities on the lattice parameter of PuN *J. Nucl. Sci. Technol.* **19** 852–4
[26] Fialho M, Lorenz K, Magalhães S, Redondo-Cubero A, Rodrigues J, Santos N F, Monteiro T and Alves E 2012 Optical doping of $Al_xGa_{1-x}N$ compounds by ion implantation of Tm ions *AIP Conf. Proc.* **1496** 63–66
[27] Magalhães S, Lorenz K, Franco N, Barradas N P, Alves E, Monteiro T, Amstatt B, Fellmann V and Daudin B 2010 Effect of annealing on AlN/GaN quantum dot heterostructures: advanced ion beam characterization and x-ray study of low-dimensional structures *Surf. Interface Anal.* **42** 1552–5
[28] Lorenz K, Franco N, Alves E, Pereira S, Watson I M, Martin R W and O'Donnell K P 2008 Strain relaxation during AlInN growth on GaN *J. Cryst. Growth* **310** 4058
[29] Darakchieva V, Xie M-Y, Tasnádi F, Abrikosov I A, Hultman L, Moneman B, Kamimura J and Kishino K 2008 Lattice parameters, deviations from Vegard's rule, and E_2 phonons on InAlN *Appl. Phys. Lett.* **93** 261908
[30] Kasper E, Werner J, Oehme M, Escoubas S, Burle N and Schulze J 2012 Growth of silicon based germanium tin alloys *Thin Solid Films* **520** 3195–200
[31] Werner J, Oehme M, Schirmer A, Kasper E and Schulze J 2012 Molecular beam epitaxy grown GeSn p-i-n photodetectors integrated on Si *Thin Solid Films* **520** 3361–4
[32] Magalhães S, Fialho M, Peres M, Lorenz K and Alves E 2016 Quantitative x-ray diffraction analysis of bimodal damage distributions in Tm implanted $Al_{0.15}Ga_{0.85}N$ *J. Phys. D: Appl. Phys.* **49** 135308
[33] Magalhães S, Cabaço J S, Mateus R, Nd D, Faye D R, Peres P M, Lorenz K, Díaz-Guerra C, Araújo J P and Alves E 2021 Crystal mosaicity determined by a novel layer deconvolution Williamson-Hall method *CrystEngComm* **23** 2048–62
[34] Salgado J C, Faye D N, Araujo J P, Alves E and Magalhães S 2021 Simulating the effect of Ar^+ energy implantation on strain propagation in AlGaN *J. Appl. Phys.* **54** 245301
[35] Fialho M, Magalhães S, Rodrigues J, Chauvat M P, Ruterana P, Monteiro T, Lorenz K and Alves E 2018 Defect formation and optical activation of Tb implanted $Al_xGa_{1-x}N$ films using channeled implanted at different temperatures *Surf. Coat. Technol.* **355** 29–39
[36] Mendes P, Lorenz K, Alves E, Schwaiger S, Scholz F and Magalhães S 2019 Measuring strain caused by ion implantation in GaN *Mat. Sci. Semcond. Proc.* **98** 95–99
[37] Jozwik P, Magalhães S, Ratajczak R, Mieszczynski C, Sequeira M, Turos A, Böttger R, Heller R, Lorenz K and Alves E 2019 RBS/C, XRR and XRD of damage buildup in Er-implanted ZnO *Phys. Status Solidi* b **256** 1800364
[38] Magalhães S, Cabaço J S, Araujo J P and Alves E 2021 Multiple reflection optimization package for x-ray diffraction *CrystEngComm* **23** 3308–18
[39] Teixeira B M S, Timopheev A A, Caçoilo N, Cuchet L, Mondaud J, Childress J R, Magalhães S, Alves E and Sobolev N A 2020 Ar^+ ion irradiation of magnetic tunnel junction multilayers: impact on the magnetic and electrical properties *J. Phys. D: App. Phys.* **53** 455003
[40] Marciel A *et al* 2021 Molybdenum oxide thin films grown on flexible ITO-coated PET substrates *Materials* **14** 821
[41] Barradas N P, Jeynes C and Webb R P 1997 Simulated annealing of Rutherford backscattering data *Appl. Phys. Lett.* **71** 291–3
[42] Chu W-K, Mayer J V and Nicolet M-A 1978 *Backscattering Spectrometry* (New York: Academic)
[43] More J J 1978 The Levenberg-Marquardt algorithm: Implementation and theory *Numerical Analysis* (*Lecture Notes in Mathematics*) ed G A Watson vol 630 (Berlin: Springer) (https://doi.org/10.1007/BFb0067700)
[44] Holý V, Pietsch U and Baumbach T 1999 *High-Resolution X-ray Scattering from Thins Films and Multilayers* (Berlin: Springer)
[45] Hammond C 2015 *The Basics of Crystallography and Diffraction* 4th edn (Oxford: Oxford University Press)
[46] Vegard L 1921 Die Konstitution der Mischkristalle und die Raumfüllung der atome *Z. Phys. Chem.* **5** 17–26
[47] Sadd M H 2004 *Elasticity: Theory, Applications, and Numerics* 1st edn (New York: Academic)
[48] Moram M A and Vickers M E 2009 X-ray diffraction of III-nitrides *Rep. Prog. Phys.* **72** 036502
[49] Metzger T *et al* 1998 Defect structure of epitaxial GaN films determined by transmission electron microscopy and triple axis-x-ray diffractometry *Phil. Mag.* A **77** 1013–25
[50] Brent R 1973 *Algorithms for Minimization without Derivatives* (Englewood Cliffs, NJ: Prentice-Hall)
[51] Forsythe G E, Malcolm M A and Moler C B 1976 *Computer Methods for Mathematical Computations* (Englewood Cliffs, NJ: Prentice-Hall)
[52] Magalhães S, Barradas N P, Alves E, Watson I M and Lorenz K 2012 High precision determination the InN content of $Al_{1-x}In_xN$ thin films by Rutherford backscattering spectrometry *Nucl. Instrum. Methods Phys. Res.* B **273** 105–8
[53] Vasin A S, Oliveira F, Cerqueira M F, Schulze J and Vasilevskiy M I 2018 Structural and vibrational properties of Sn_xGe_{1-x}: modelling and experiments *J. Appl. Phys.* **124** 035105
[54] Xu C, Senaratne C L, Culbertson R J, Kouvetakis J and Menéndez J 2017 Deviation from Vegard's law in semiconductor thin films measured with x-ray diffraction and Rutherford backscattering: the $Ge_{1-y}Sn_y$ and $Ge_{1-x}Si_x$ cases *J. Appl. Phys.* **122** 125702
[55] Sadao A 2009 *Properties of Semiconductor Alloys: Group-IV, III-V and II-VI Semiconductors* vol 28 (New York: Wiley)
[56] Wang W, Zhou Q, Dong Y, Tok E S and Yeo Y-C 2015 Critical thickness for strain relaxation of $Ge_{1-x}Sn_x$ ($x \leqslant 0.17$) grown by molecular beam epitaxy on Ge (001) *Appl. Phys. Lett.* **106** 232106
[57] Alam M M, Wagatsuma Y, Okada K, Hoshi Y, Yamada M, Hamaya K and Sawano K 2019 Critical thickness of strained $Si_{1-x}Ge_x$ on Ge (111) and Ge-on-Si (111) *Appl. Phys. Exp.* **12** 081005

[58] Yang J, Hu H, Miao Y, Dong L, Wang B, Wang W, Su H, Xuan R and Zhang H 2019 High-quality GeSn layer with Sn composition up to 7% grown by low-temperature magnetron sputtering for optoelectronic application *Materials* **12** 2662
[59] Stanchu H V, Kuchuk A V, Mazur Y, Pandey K, de Oliveira F M, Benamara M, Teodoro M D, Yu S-Q and Salamo G J 2021 Quantitative correlation study of dislocation generation, strain relief and Sn outdiffusion in thermally annealed GeSn epilayers *Cryst. Growth Des.* **21** 1666–73
[60] Zhang L, Song Y, von den Driesch N, Zhang Z, Buca D, Grützmacher D and Wang S 2020 Structural property study for GeSn thin films *Materials* **13** 3645
[61] Parratt L G 1954 Surface studies of solids by total reflection x-rays *Phys. Rev.* **95** 359–69
[62] Mâaza M, Gibaud A, Sella C, Pardo B, Dunsteter F, Corno J, Bridou F, Vignaud G, Désert A and Menelle A 1999 X-ray scattering by nano-particles within granular thin films, investigation by grazing angle x-ray reflectometry *Eur. Phys. J.* B **7** 339–45
[63] Stanchu H V, Kuchuk A V, Mazur Y I, Margetis J, Tolle J, Yu S-Q and Salamo G J 2020 Strain suppressed Sn incorporation in GeSn epitazially grown on Ge/Si(001) substrate *Appl. Phys. Lett.* **16** 232101
[64] Zaima S, Nakatsuka O, Taoka N, Kurosawa M, Takeuchi W and Sakashita M 2015 *Sci. Technol. Adv. Mater.* **16** 043502
[65] Wirths S, Geiger R, von den Driesch N, Mussler G, Stoica T, Mantl S, Ikonic Z, Luysberg M I, Chiuss S and Harmann J M 2015 Lasing in direct-bandgap GeSn alloy grown on Si *Nat. Phton.* **9** 88